



Pt- and Ru-decorated metal organic framework as a trifunctional material for water electrolysis and hydrogen fuel cell applications

Terrence Mothlathlo^{1,2} · Kwena D. Modibane^{1,2} · Kabelo E. Ramohlolwa^{1,3} · Gobeng R. Monama^{1,3} · Jianwei Ren⁴

Received: 27 May 2025 / Accepted: 18 October 2025
© The Author(s), under exclusive licence to Springer Nature B.V. 2026

Abstract

The development of efficient hydrogen fuel cell (HFC) and water-splitting electrocatalysts was considered critical for advancing clean energy technologies. In this study, platinum (Pt) and ruthenium (Ru) were incorporated into copper zeolitic imidazolate framework (CuZIF) using an electroless plating method. Comprehensive characterization through Fourier transform infrared spectroscopy, thermogravimetric analysis, X-ray diffraction, and scanning electron microscopy coupled with energy dispersive X-ray spectroscopy confirmed the successful synthesis of pristine CuZIF and the metallic-incorporated Pt@CuZIF and Ru@CuZIF. Electrochemical measurements were carried out in 0.1 M potassium hydroxide (KOH) to evaluate the catalytic activity of the prepared materials in water electrolysis for the hydrogen evolution reaction (HER) and the oxygen evolution reaction (OER), as well as in HFC testing. Pt@CuZIF demonstrated enhanced catalytic activity for both HER and OER, with Tafel slopes of 118 and 118.5 mV dec⁻¹, respectively, suggesting a Volmer–Heyrovsky mechanism, and overpotentials of 345 and 474 mV. Electrochemical impedance spectroscopy (EIS) further revealed that both HER and OER benefited from Pt@CuZIF due to its low charge transfer resistance and high capacitance value. HFC measurements showed that Pt@CuZIF exhibited excellent performance and stability, with a discharge voltage of 0.13 V, an energy density of 68.42 Wh kg⁻¹, and a power density of 205.26 W kg⁻¹. In comparison, Ru@CuZIF exhibited a discharge voltage of 0.17 V, an energy density of 90.91 Wh kg⁻¹, and a power density of 272.73 W kg⁻¹. Overall, Pt@CuZIF was considered the most promising material for application in both water electrolysis and HFCs.

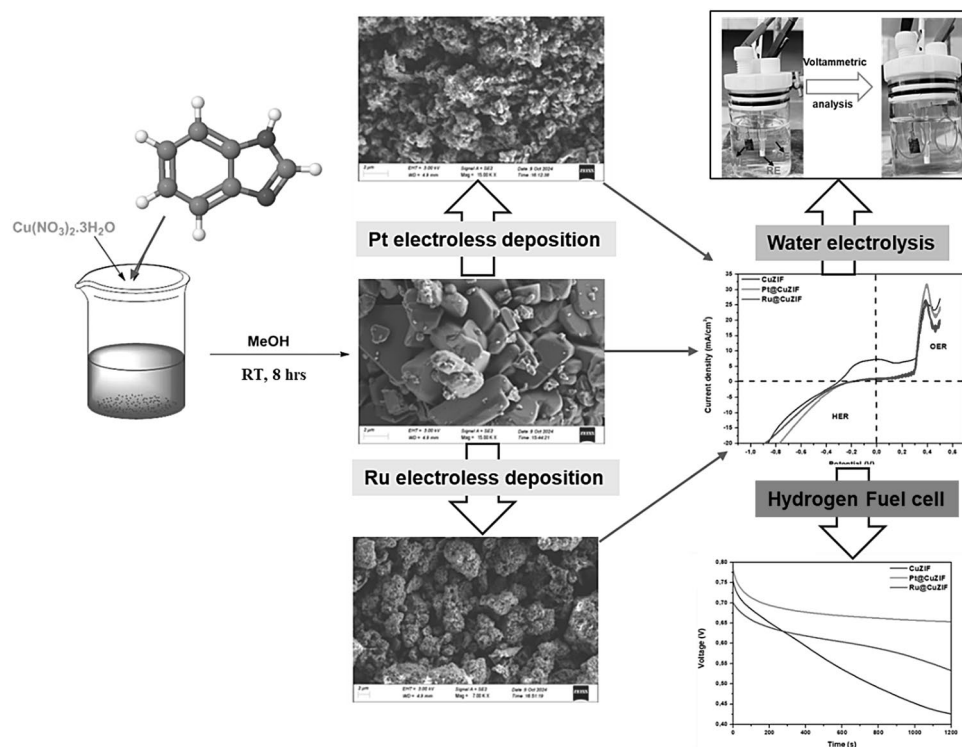
✉ Kwena D. Modibane
kwena.modibane@ul.ac.za

¹ Department of Chemistry, School of Physical and Mineral Sciences, Faculty of Science and Agriculture, University of Limpopo (Turfloop), Polokwane 0727, Sovenga, South Africa

² DSI-NRF SARCHI Chair in Photoelectrocatalytic Hydrogen Production, Department of Chemistry, School of Physical and Mineral Sciences, University of Limpopo (Turfloop), Polokwane 0727, Sovenga, South Africa

³ Faculty of Science, SensorLab (University of the Western Cape Sensor Laboratories), University of the Western Cape, Bellville, Cape Town 7535, South Africa

⁴ Department of Chemical Engineering, University of Pretoria, Hatfield, Pretoria 0028, South Africa

Graphical Abstract

Keywords Pt@CuZIF · Ru@CuZIF · Copper zeolithic imidazolate framework · HER electrocatalyst · OER electrocatalyst · Hydrogen fuel cell performance · Trifunctional catalyst

1 Introduction

The growing demand for clean energy poses a pressing environmental challenge, aiming to reduce both pollution and greenhouse gas emissions [1]. Hydrogen fuel cells (HFCs) stand out as an appealing solution due to their renewable character, high efficiency, zero-emission byproduct (water), and superior energy density compared to gasoline [2, 3]. These advantages position HFCs for a wide spectrum of uses from portable devices and transportation to large-scale stationary power systems [4, 5]. Additionally, HFCs are nearly twice as efficient as fossil fuels [4]. A key step in sustainable hydrogen (H_2) production is electrocatalytic water splitting (EWS), which involves the oxygen evolution reaction (OER) at the anode and hydrogen evolution reaction (HER) at the cathode [6]. EWS produces high-purity H_2 with minimal impurities, making it one of the most cost-effective and scalable routes to hydrogen energy [7]. However, HER and OER remains the major kinetic bottleneck due to its sluggish multi-electron dynamics. Noble metal catalysts such as IrO₂, PtO₂, and RuO₂ exhibit superior catalytic activity, but their scarcity and high-cost limit large-scale application [8]. Recent studies have explored

low-cost alternatives, including ceramic- and carbon-based electrocatalysts, to address these limitations. For instance, samarium-doped SnFe₂O₄ spinels enhance OER activity with reduced overpotential and improved kinetics [9], while Mo-doped ZnAl₂O₄ spinel nanorods directly grown on carbon fiber exhibit bifunctional catalytic properties with high stability [10]. Similarly, nanostructured carbon films and diamond-like carbon composites provide durable, conductive supports for electrocatalysis [11, 12]. In addition, MOF-derived metal oxyhydroxide layers with abundant oxygen defects have been shown to significantly enhance OER efficiency due to improved active-site exposure and electrode-electrolyte interactions [13]. Alongside these materials, polymer electrolytes continue to play a crucial role. Hydrocarbon- and perfluorocarbon-based polymers have been widely employed in electrolyzers and HFCs [5, 14]. Among them, perfluorosulfonic acid (PFSA) membranes, especially Nafion, remain the benchmark due to their high proton conductivity, as well as their excellent thermal and mechanical stability [15–17]. The sulfonic acid groups in Nafion's side chains impart hydrophilicity, enabling water uptake and facilitating proton transport [18]. However, several challenges still hinder HFC commercialization, particularly

sluggish electrode kinetics where the oxygen reduction reaction (ORR) at the cathode is significantly slower than hydrogen oxidation at the anode [19–21].

Metal organic frameworks (MOFs) have received considerable interest over the past decade and have found diverse applications including gas separation, catalysis, and energy conversion for HER, OER, and HFCs [22–24]. In the past decade, porous MOFs have experienced remarkable growth due to their exceptional surface area, tunable pore structures, and chemical versatility [25, 26]. Creating additional proton transfer routes by employing MOFs as proton carriers can greatly enhance the H_2 production rate of electrolyzers and the proton conductivity of HFCs [27].

For instance, Zhu et al. first reported a polymer/MOF composite proton exchange membrane (PEM) made of MOF-1 and polyvinylpyrrolidone (PVP), which demonstrated improved proton conductivity [28]. Additionally, other polymer/MOF composite PEMs, such as Nafion/MOF-808 (zirconium-based), sulfonated poly(ether ether ketone) (SPEEK)/MIL-101 (chromium-based), and sulfonated poly(ethersulfone) (SPES)/MIL-53 (aluminum-based), have also been successfully developed [5]. In HER, MOFs serve as tunable platforms for optimizing active sites and improving H_2 adsorption/desorption, often through the integration of transition metals or heteroatoms. In OER, they facilitate oxygen (O_2) evolution via customizable catalytic sites and adjustable electronic structures [29–31]. For instance, Huang and colleagues utilized hexaiminohexaaazatrinaphthalene (HAHATN) as a ligand to design $M_{2^3}(M_{13}\cdot HAHATN)_2$ MOFs featuring an additional metallic center ($M\text{-}N_2$). The optimized structure, $Ni_3(Ni_3\cdot HAHATN)_2$, demonstrated a 115 mV overpotential at a current density of 10 mA cm^{-2} and a Tafel slope of 45.6 mV dec^{-1} for the HER in a 0.1 M KOH solution [32]. Similarly, Li and colleagues investigated a series of Fe/Ni MOFs derived from the MIL-53 structure, adjusting the Fe/Ni molar ratios to create effective OER catalysts. The optimized $Fe/Ni_{2.4}/Co_{0.4}\text{-MIL-53}$ exhibited a current density of 20 mA cm^{-2} at an overpotential of 236 mV, along with a low Tafel slope of 52.2 mV dec^{-1} [33]. Despite these advancements in utilizing MOFs as potential electrocatalysts for HER, OER, and HFCs, achieving enhanced catalytic activity and long-term durability remains a significant challenge [34, 35]. Therefore, there is a need to develop MOF-based supports that can serve as efficient and stable electrocatalysts.

In this study, copper zeolitic imidazolate framework (CuZIF) was chosen as the support material due to its large surface area, microporosity, and robust thermal/chemical stability, which provide abundant active sites and enable efficient electron and mass transport [25, 26, 36]. To further improve its catalytic performance, Pt (Platinum) and Ru (Ruthenium) were selectively incorporated into CuZIF

because of their complementary catalytic properties. Pt is widely recognized for its superior HER activity and stability in alkaline media [21, 35], while Ru exhibits excellent OER kinetics at comparatively lower cost than Pt [36–38]. The synergistic interaction between Pt or Ru with the CuZIF support is therefore expected to yield a trifunctional catalyst with enhanced activity toward HER, OER, and HFC applications.

2 Experimental

2.1 Materials

Copper nitrate trihydrate ($Cu(NO_3)_2\cdot 3H_2O$), benzimidazole ($C_{12}H_{12}N_4O_3$), sodium hypophosphite ($NaPO_2H_2$), ruthenium (III) chloride ($RuCl_3$), platinum (II) chloride ($PtCl_2$), N-methyl-2-pyrrolidinone (NMP), nickel foam (Ni-foam), carbon black and Polyvinylidene fluoride (PVDF ($C_2H_2F_2$)) were purchased from Sigma Aldrich, South Africa. 32% hydrochloric acid (HCl), ethanol (EtOH), methanol (MeOH), 25% ammonia solution (NH_4OH), Ammonium chloride (NH_4Cl), and potassium hydroxide (KOH) were purchased from Rochelle chemicals. All chemicals were used as received.

2.2 Synthesis

2.2.1 Synthesis of CuZIF MOF

The synthesis procedure was based on previous literature with some alterations [39]. In a separate beaker, 0.8 g of copper nitrate trihydrate ($Cu(NO_3)_2\cdot 3H_2O$) was dissolved in 3 mL of methanol and 5.5 g benzimidazole in 20 mL methanol, and the two solutions were mixed and stirred (400 rpm) at room temperature for 6 h. The purple-brownish precipitate obtained was acquired by centrifugation, washed three times with distilled water and methanol, and then dried at 80 °C for 24 h.

2.2.2 Synthesis of Pt@CuZIF and Ru@CuZIF materials

The materials were prepared using the electroless plating method [40]. Briefly, the plating solution was created by dissolving 1 g of metal chloride ($PtCl_2$ or $RuCl_3$) in 2 mL of 32% HCl and 10 mL of ultra-pure water, respectively, followed by heating at 50 °C for 30 min with constant stirring at 300 rpm. After the metal chloride has completely dissolved, 80 mL of 28% NH_4OH and 27 g of NH_4Cl were added, respectively. The mixture was then transferred to a 500 mL volumetric flask and filled to the mark with ultra-pure water. The electroless plating bath was prepared by

adding 25 mL of 5 g L⁻¹ NaPO₂H₂ as a reducing agent to a 2.5 g batch of CuZIF, which was stirred at 300 rpm for 30 min at 50 °C in a separate bath to prevent decomposition. Finally, 25 mL of the plating solution was added to the bath, and the mixture was stirred for 30 min to plate the Pt and Ru onto the composite surface. The mixture was then filtered, washed with ultra-pure water, and dried overnight at 80 °C to obtain the product. The product obtained from PtCl₂ and RuCl₃ were named Pt@CuZIF and Ru@CuZIF with weight percentages of 1.87 wt% of Pt and 1.22 wt% of Ru from EDX analysis, respectively (Scheme 1).

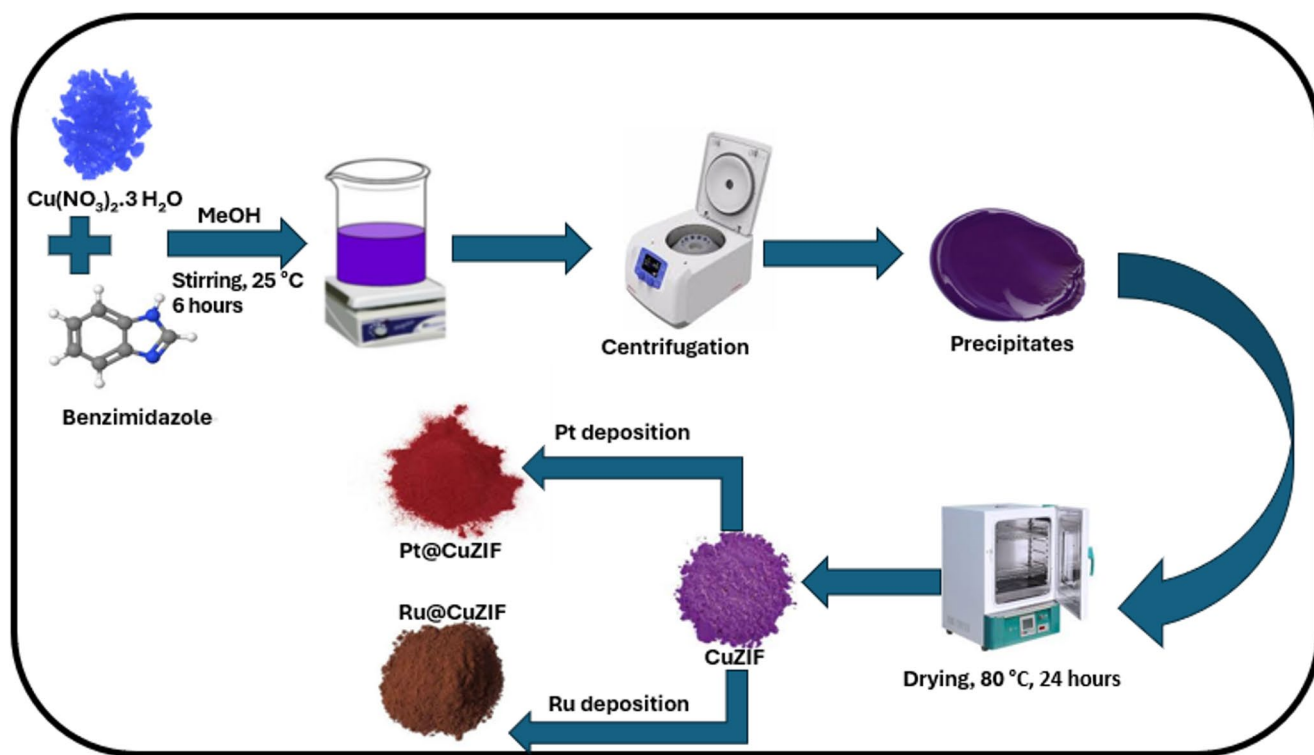
2.3 Characterization techniques

Various analytical techniques have been used to characterise the synthesised materials. Fourier-transform infrared spectroscopy (FTIR) using Spectrum II spectrometer (PerkinElmer) recorded from 400 to 4000 cm⁻¹ with minimum of 32 scans and resolution of 4 cm⁻¹ at room temperature was used to analyse the formation and characteristic peaks of the materials. X-ray diffraction (XRD) using (XRD Philips PW 1830, Cu-K α radiation, $\lambda=1.5406\text{ \AA}$) was used to investigate the phase structure of the materials at 35 kV and 40 mA. The thermal stability of the materials was evaluated by thermogravimetric analyser (STA) using PerkinElmer 6000 instrument coupled with a PolyScience digital temperature controller under nitrogen gas purged at 20 mL min⁻¹ flow rate using aluminium (melting point=660 °C)

and indium (melting point=156.6 °C) to calibrate the system. Samples with the weight ranging from 1 to 4 mg were subjected to the heating temperature (30–700 °C) and constant heating rate (10 °C min⁻¹), and the data was analyzed using Pyris software. The structure and morphology of the materials were examined by scanning electron microscopy/energy dispersive X-ray analysis (SEM/EDX) using (SEM, Auriga Carl Zeiss) conducted at a voltage of 30 kV. EDX spectra were collected using EDAX liquid nitrogen cooled lithium doped silicon detector.

2.4 Electrochemical measurements

Electrochemical measurements were carried out on a Bio-logic SP150 Electro-chemical workstation equipped with a three-electrode assembly. The reference and counter electrodes of silver/silver chloride (Ag/AgCl) and Pt wire were used, while modified Ni-foam was used as a working electrode in the setup. To fabricate the working electrode, firstly, the Ni-foam substrate was treated by sonication in 3 M HCl, distilled water, and EtOH respectively, for 15 min individually. The Ni foam pieces were then dried at 60 °C for 2 hours. Finally, the ink was prepared by mixing 15 mg of active material, 3 mg of carbon black, and 2 mg of PVDF in 200 μL of NMP. The solution was sonicated overnight to ensure thorough dispersion. The ink was drop-cast onto the nickel foam of $0.5 \times 1\text{ cm}^2$ and was left to be dried at 60 °C for 3 h [41], and the coated amount present on the Ni-foams



Scheme 1 Preparation of CuZIF, Pt@CuZIF and Ru@CuZIF procedure

were found to be 1.87, 1.90 and 1.89 mg for CuZIF, Pt@CuZIF and Ru@CuZIF, respectively.

3 Results and discussion

3.1 Structural properties

FTIR analysis was conducted to identify the functional groups present in CuZIF, Pt@CuZIF, and Ru@CuZIF, and the spectra of the prepared materials are depicted in Fig. 1 (a). CuZIF displayed vibrations around 1200, 1640, and 3050 cm^{-1} , corresponding to C-N, C = C, and C-H bonds, respectively [42]. Furthermore, the benzimidazole organic ligand exhibits a C-H stretching vibration at 3100–3000 cm^{-1} , a C = C stretch at 1600–1500 cm^{-1} , and a strong N-H peak around 3500–2500 cm^{-1} , consistent with the reported work by Huang et al. [43]. Moreover, Cu-N stretching appeared between 600 and 700 cm^{-1} [44], and C = N around 1604 cm^{-1} [45]. Pt@CuZIF and Ru@CuZIF spectra closely

resembled that of CuZIF, with slight shifts in peak intensity attributed to the interaction of Pt and Ru with the framework. Notably, in the region of 1200–1100 cm^{-1} , both Pt@CuZIF and Ru@CuZIF exhibit nearly identical features yet differ significantly from pristine CuZIF. Depositing noble metals perturbs the M-N-C environment similarly in both Pt@CuZIF and Ru@CuZIF through comparable electron donation and coordination to the imidazolate N-sites, causing their band shapes and positions to converge [46]. By contrast, in CuZIF the linker environment is less perturbed, resulting in distinct spectral features. Assignments of 1175–1145 cm^{-1} to C-N stretches in ZIFs are well established [47, 48]. These observations are in good agreement with recent reports on FTIR features of ZIF-based and noble-metal-modified frameworks, where similar peak shifts and M-N-C perturbations were observed in Cu- and Pt/Ru-containing ZIF systems [9, 49].

Thermal gravimetric analysis (TGA), as shown in Fig. 1 (b), provides valuable information on the thermal stability and composition of the material. CuZIF shows two distinct

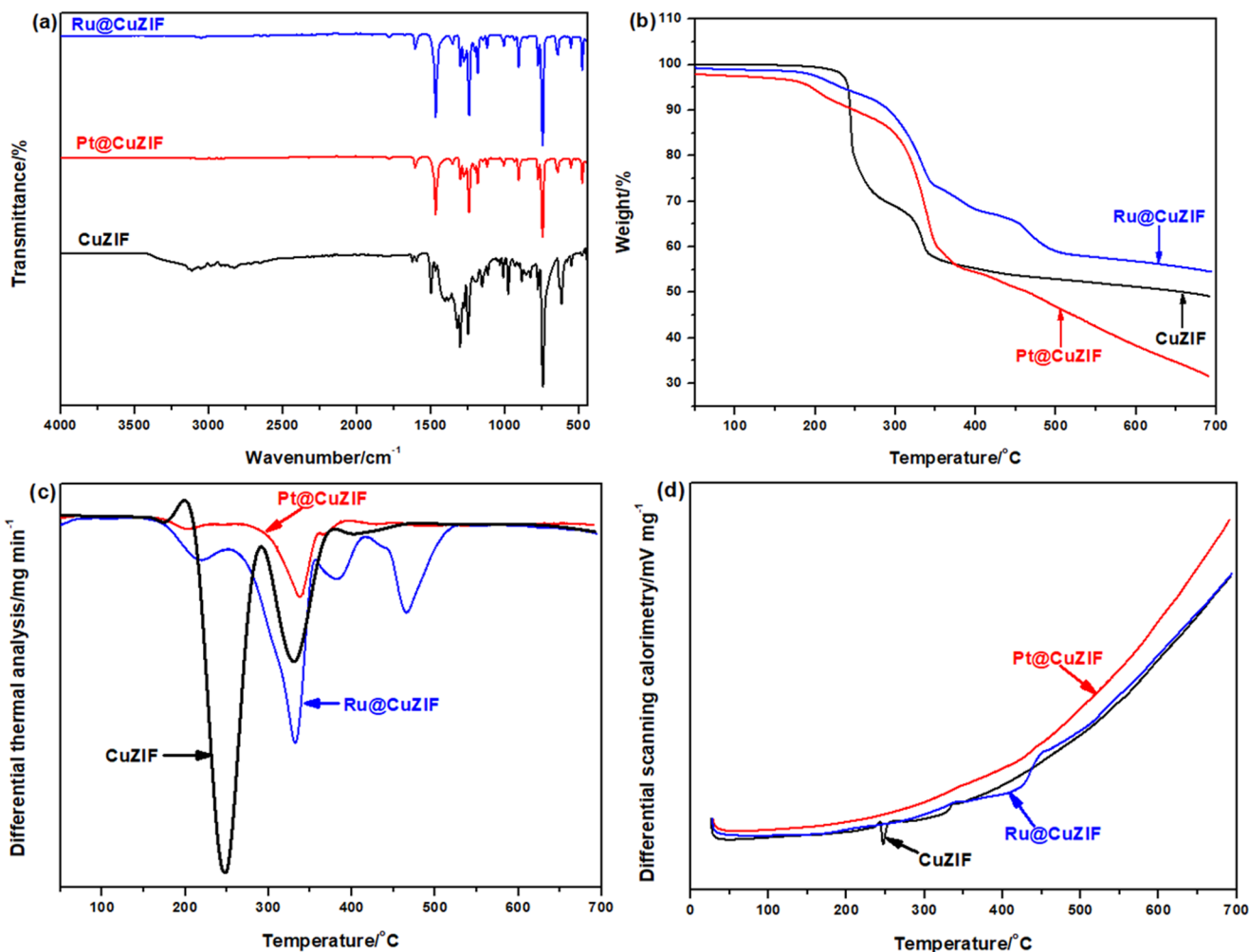


Fig. 1 **a** FTIR spectra, **b** TGA curves, **c** DTA curves, and **d** heat flow of CuZIF, Pt@CuZIF and Ru@CuZIF

stages of thermal degradation across the experimental temperature range, indicating the decomposition of different components. The initial weight loss of 30 wt% occurring around 280 °C is due to the elimination of trapped guest molecules and unreacted species such as solvents and moisture within the porous cavities of the CuZIF structure [42]. A further weight loss of 3 wt% around 345 °C can be attributed to the decomposition of organic linkers or ligands in the CuZIF structure [50]. Pt@CuZIF exhibits similar behavior to CuZIF up to 200 °C but then begins to lose weight more gradually. The decomposition of 9 wt% occurs earlier around 200 °C, followed by a larger weight loss of 27 wt% between 300 and 350 °C, and a continued loss of 35 wt% up to about 700 °C. Ru@CuZIF shows a similar trend, with a smaller weight loss of 17 wt% between 300 and 350 °C, confirming that similar organic groups are present in their structure [51]. The earlier onset of weight loss in Pt@CuZIF and Ru@CuZIF compared to pristine CuZIF is noteworthy. Early loss at 200 °C in metal-decorated ZIFs is commonly due to the desorption or decomposition of surface/porous adsorbates introduced during plating and catalytic lowering of ligand-dehydrogenation temperatures by Pt and Ru nanoparticles, which initiate minor mass loss before the backbone deconstructs. Additionally, hypophosphite-type reducers and related phosphorus-containing species often employed in electroless plating are known to decompose in the 200–320 °C range, producing volatile species consistent with the small early step observed in both Pt@CuZIF and Ru@CuZIF [52].

The differential thermal analysis (DTA) and differential scanning calorimetry (DSC) results in Fig. 1 (c, d) show a strong correlation with the TGA analysis [53]. In Fig. 1 (c) which represent DTA, there is a large, sharp endothermic peak around 250 °C, which is due to the decomposition of the ZIF framework or the desorption of coordinated molecules. Additionally, an endothermic peak between 350 °C occurs due to the absorption of heat as the frameworks of the MOF material collapse [50, 54]. The curve then stabilizes suggesting that most thermal transformations have completed around 400 °C. For Pt@CuZIF, the main thermal event occurs between 300 and 400 °C, as indicated by the endothermic peak. This thermal event suggests that the presence of Pt alters the thermal stability of CuZIF, likely by stabilizing the structure or delaying its decomposition [55]. For Ru@CuZIF, a distinct endothermic peak occurs around 350 to 400 °C, showing that the Ru also affects the thermal stability of the CuZIF [56]. The peak for Ru@CuZIF is broader compared to Pt@CuZIF, suggesting that the interaction between CuZIF and Ru is slightly different and may involve more complex thermal transformations or multiple stages of decomposition. In Fig. 1 (d), which represent DSC, CuZIF shows a gradual increase in heat flow as

the temperature increases. There is a notable event around 250 °C which indicate a phase change, structural rearrangement, or degradation of the CuZIF structure [57]. Pt@CuZIF exhibits a significantly higher heat flow compared to CuZIF and Ru@CuZIF, suggesting that the incorporation of Pt leads to greater thermal changes or heat release upon heating. The sharp increase in heat flow as temperature rises beyond 450 °C indicate stronger interactions or enhanced decomposition [58]. Ru@CuZIF is somewhat similar to CuZIF, though it shows a slightly higher heat flow and a sharper change around 450 °C, indicating the influence of Ru on the thermal properties.

Figure 2 (a) shows the XRD patterns of CuZIF, Pt@CuZIF, and Ru@CuZIF. By comparing the resulting patterns, it was observed that all peaks associated with the CuZIF structure also appear in the Pt@CuZIF and Ru@CuZIF, indicating that the incorporation of Pt and Ru did not compromise the overall structural integrity of the CuZIF framework. The CuZIF pattern displays a series of sharp peaks at $2\theta = 7.90, 10.06, 13.83, 15.47, 20.65$, and 26.32° , corresponding to the (100), (110), (200), (210), (211), and (220) planes, respectively, which are consistent with previously reported sodalite-type ZIF structures [51, 59, 60]. In contrast, Pt@CuZIF and Ru@CuZIF patterns exhibit a reduction in peak intensity and some peak broadening compared to pristine CuZIF. Moreover, both materials display two distinct peaks at around $2\theta = 10.30^\circ$ and 23.92° , which can be indexed to the (001) and (002) planes [61–63]. Introducing metal species into CuZIF defect the framework, which results in broader background and lower intensity peaks. Numerous ZIF-metal studies have reported decreased crystallinity and disappearance of characteristic peaks after loading Pt, Ru, or other nanoparticles [64–66]. In addition, low-loading nanoparticles frequently evade direct detection in XRD, while the original ZIF peaks weaken as crystallite size decreases and structural defects increase [67]. The observed decrease in intensity and peak broadening in Pt@CuZIF and Ru@CuZIF therefore suggests partial disruption or distortion in the framework caused by Pt and Ru incorporation [68]. Moreover, the crystallite size (D) was calculated using the Debye-Scherrer in Eq. 1 [69]:

$$D = k\lambda/\beta \cos \theta \quad (1)$$

where K and β represent the Debye-Scherrer constant and the full width at half maximum (FWHM), respectively, θ denotes the diffraction angle, and λ is the wavelength of the Cu-K α with a value of 1.5406 Å. The D values of CuZIF, Pt@CuZIF, and Ru@CuZIF were obtained to be 110.61, 28.86 and 46.92 nm, respectively. The strain (ϵ) values were found to be 3.28×10^{-4} , 1.33×10^{-3} and 1.29×10^{-3} and dislocation densities were determined to be 0.09, 1.80 and 1.56

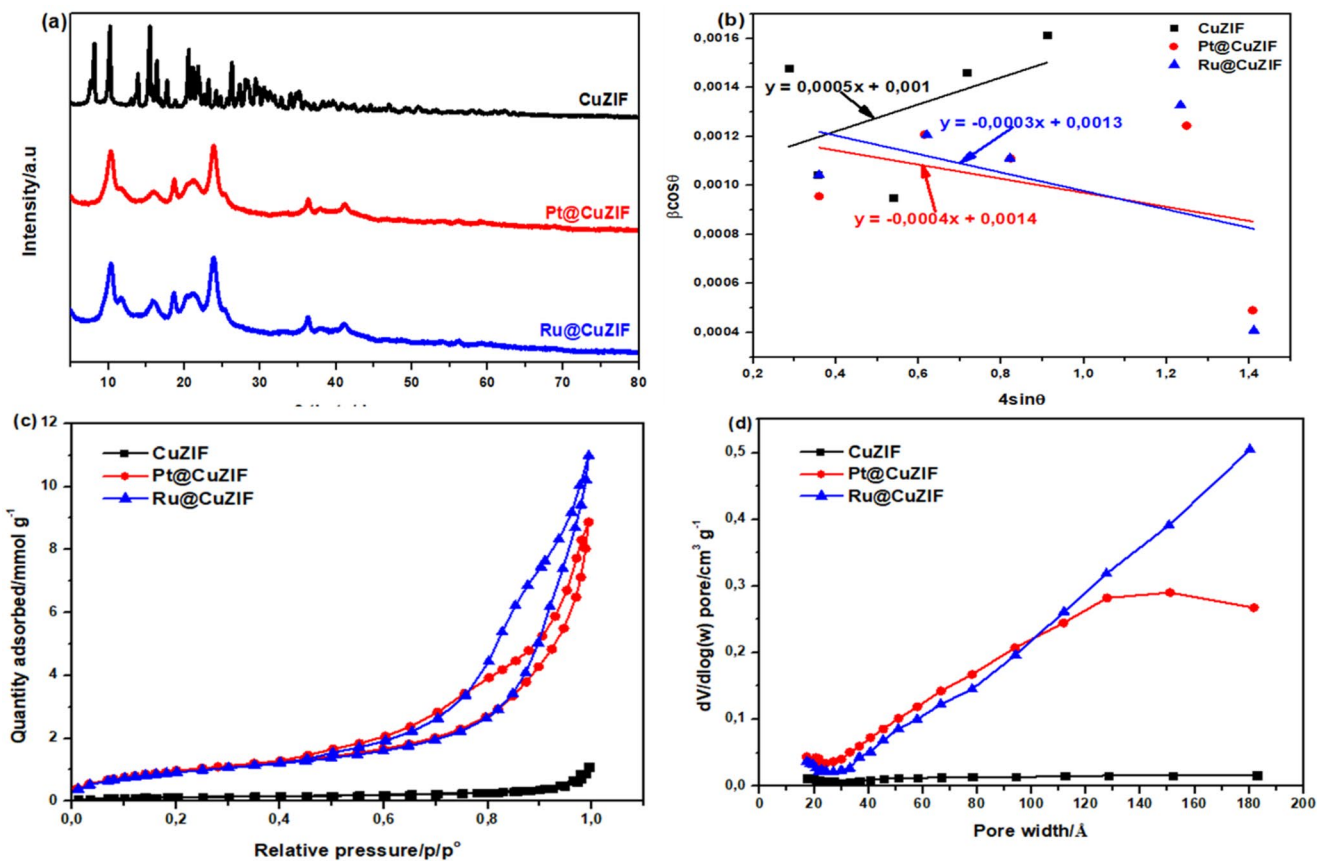


Fig. 2 **a** XRD pattern, **b** Williamson-Hall plot, **c** BET isotherms and **d** pore volume distribution of CuZIF, Pt@CuZIF and Ru@CuZIF

Table 1 XRD parameters and BET surface area of CuZIF, Pt@CuZIF and Ru@CuZIF

Materials	BET area ($\text{m}^2 \text{ g}^{-1}$)	d-space (\AA)	Dislocation density (m^{-2})	D		Strain	
				(nm)	Deybe-Sherrer	W-H	Deybe-Sherrer
CuZIF	4.91	6.57	0.09	110.61	138.65	3.28×10^{-4}	2.5×10^{-4}
Pt@CuZIF	52.02	3.28	1.80	28.86	24.33	1.33×10^{-3}	1.43×10^{-3}
Ru@CuZIF	53.87	4.40	1.56	46.92	39.62	1.29×10^{-3}	1.35×10^{-3}

m^{-2} for CuZIF, Pt@CuZIF and Ru@CuZIF, respectively. The calculated parameters are shown in Table 1. Additionally, D and ϵ values were determined using the Williamson-Hall (W-H) plot, following Eq. 2 [69, 70]:

$$\beta \cos \theta = 0.9\lambda/D \times 4\epsilon \sin \theta \quad (2)$$

The D values were calculated to be 138.65, 24.33 and 39.62 nm from the y-intercept, while ϵ values were determined to be 2.5×10^{-4} , 1.43×10^{-3} and 1.35×10^{-3} from the slopes of CuZIF, Pt@CuZIF and Ru@CuZIF, respectively. The Brunauer-Emmett-Teller (BET) nitrogen adsorption-desorption isotherms in Figure (c) and Barret-Joyner-Halenda (BJH) pore size distributions in Figure (d) revealed distinct textural properties among CuZIF, Pt@CuZIF, and Ru@CuZIF. The BET surface area and pore

volume of CuZIF, Pt@CuZIF and Ru@CuZIF were found to be 4.91, 52.02 and 53.87 $\text{m}^2 \text{ g}^{-1}$ and 0.013, 0.161 and $0.188 \text{ cm}^3 \text{ g}^{-1}$, respectively. These results confirm that metal incorporation enhances the surface accessibility and diffusion pathways of CuZIF.

3.2 Morphological characteristics

The morphology of the synthesized materials is crucial for assessing the various shapes, structures, and elemental compositions of the precursor materials, as well as for verifying the successful synthesis of the composite material [42]. Figure 3 (a-i) reveal the SEM images, EDX and particle size distributions of CuZIF, Pt@CuZIF and Ru@CuZIF. The particles in the image in Fig. 3 (a) of CuZIF exhibit well-defined edges and facets, which is characteristic of

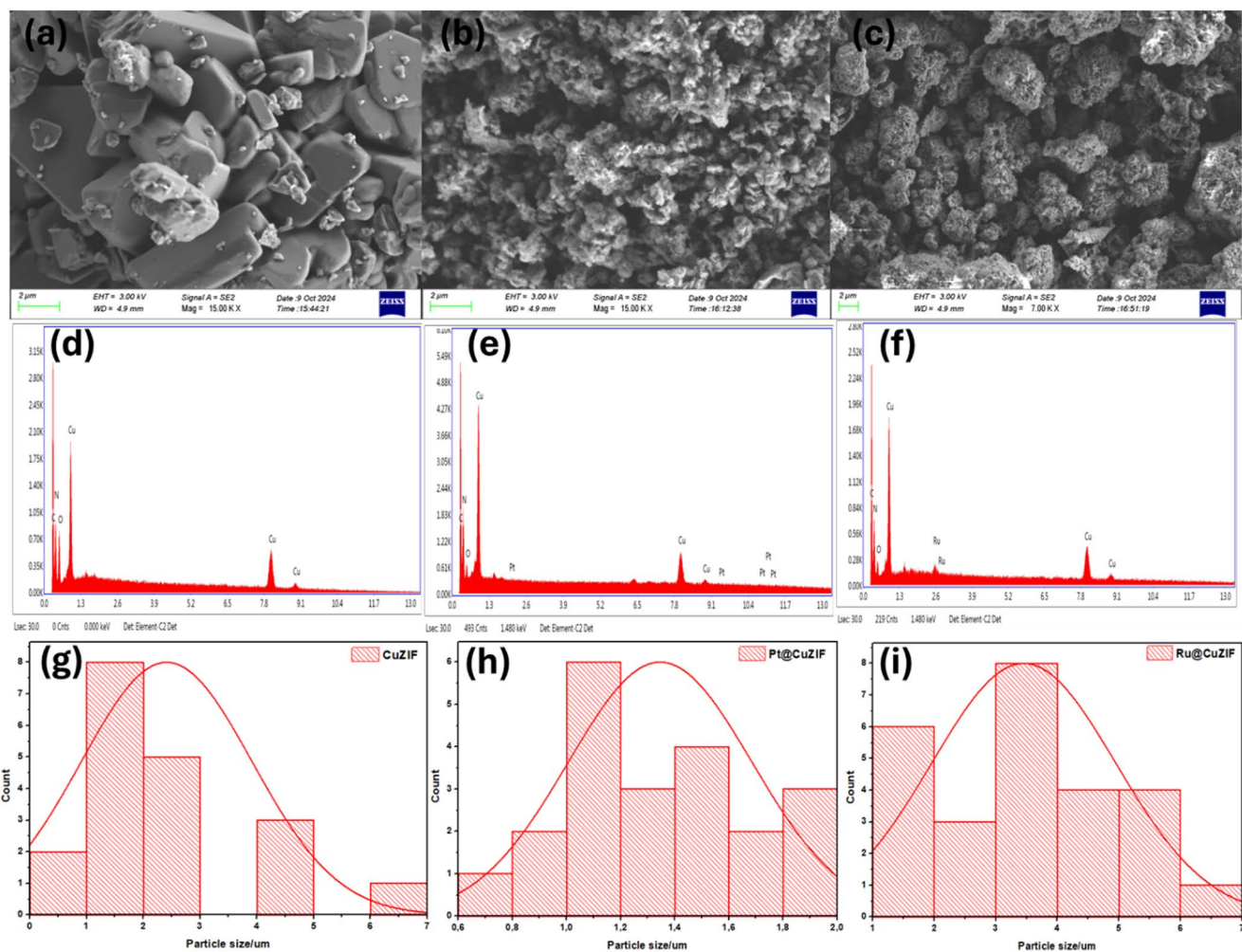


Fig. 3 SEM image of **a** CuZIF, **b** Pt@CuZIF, and **c** Ru@CuZIF, EDX of **d** CuZIF, **e** Pt@CuZIF, and **f** Ru@CuZIF, and particle size distribution of **g** CuZIF, **h** Pt@CuZIF, and **i** Ru@CuZIF

crystalline materials. This suggests that the CuZIF has formed in a regular, ordered manner [71]. The smooth surface of CuZIF indicates that its adsorptive active sites are favorable, and it can be modified to display an increased number of active sites [72]. The blocky, polyhedral shapes suggest a highly crystalline nature typical of CuZIF whereby Cu coordinate with organic linkers to form such structures [73]. The EDX in Fig. 3 (d) revealed the presence of Cu, C and N elements. Figure 3 (b) shows the morphology of Pt@CuZIF. As compared to CuZIF, the change in morphology is due to the presence of Pt, which could alter the surface structure of the CuZIF. The roughness and porosity in Pt@CuZIF are more pronounced due to the deposition of Pt, which increase the surface roughness [74]. This enhances catalytic properties of this material. The EDX in Fig. 3 (e) shows the presence of Pt, Cu, C and N elements. Figure 3 (c) represent Ru@CuZIF. The Ru nanoparticles seem to be uniformly disturbed across the CuZIF support. The surface appears to be rough, with visible granular features

indicating the presence of Ru on the surface. The particles are relatively small and well-distributed, implying that the synthesis method resulted in good dispersion [75] of Ru nanoparticles on the CuZIF surface. The EDX results in Fig. 3 (f) shows the presence of Ru, Cu, C and N elements. The particle sizes of the materials were determined to be 2.41, 1.58, and 3.45 μm for CuZIF, Pt@CuZIF and Ru@CuZIF, respectively, as shown in Table 2, and their particle distribution is shown in Fig. 3 (g-i).

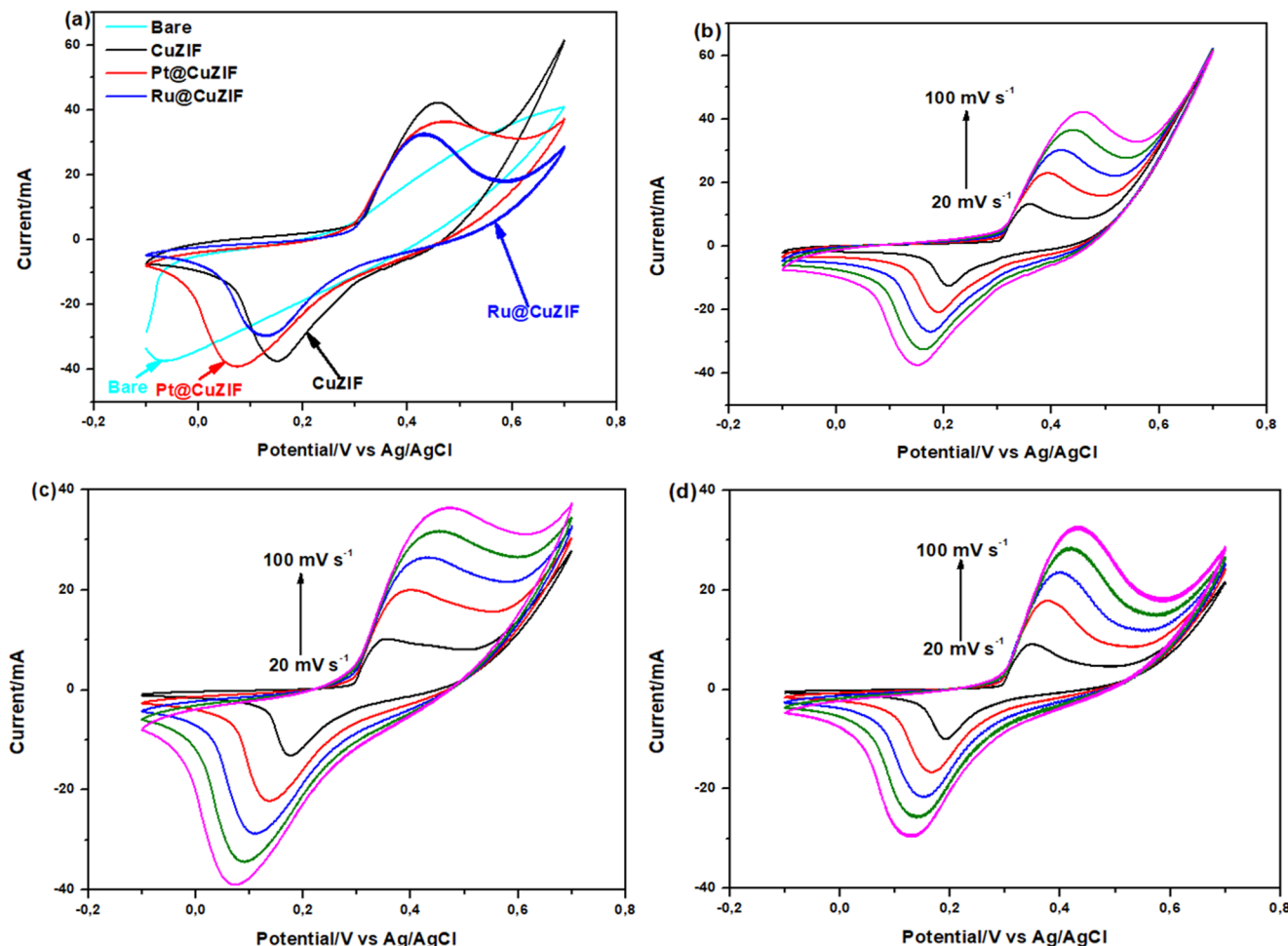
3.3 Electrochemical characterisation

3.3.1 Cyclic voltammetry studies

The electrochemical performance of nickel foam (bare), CuZIF, Pt@CuZIF and Ru@CuZIF was conducted using cyclic voltammetry in 0.1 M KOH at 100 mV s^{-1} scan rate and the cyclic voltammograms are shown in Fig. 4 (a-d). Figure 4 (a) shows the comparison cyclic voltammogram

Table 2 EDX parameters of CuZIF, Pt@CuZIF and Ru@CuZIF

Materials	Carbon (%)	Oxygen (%)	Nitrogen (%)	Copper (%)	Platinum (%)	Ruthenium (%)
CuZIF	28.50	24.32	30.68	16.50	—	—
Pt@CuZIF	37.18	20.19	30.02	10.74	1.87	—
Ru@CuZIF	28.26	19.30	38.03	13.19	—	1.22

**Fig. 4** CV curves of **a** bare, CuZIF, Pt@CuZIF and Ru@CuZIF at 100 mV s^{-1} , **b** CuZIF, **c** Pt@CuZIF and **d** Ru@CuZIF in 0.1 M KOH

of bare, CuZIF, Pt@CuZIF and Ru@CuZIF. In Fig. 4 (a), it was noted that the bare sample exhibits no anodic or cathodic peaks, while CuZIF, Pt@CuZIF, and Ru@CuZIF display both peaks. This is because the bare material does not possess active sites or conductive properties necessary to facilitate redox reactions [76], whereas CuZIF, Pt@CuZIF and Ru@CuZIF contain metal sites or catalytic components that enhance their ability to participate in electron transfer processes, leading to the observable peaks [77, 78]. CuZIF shows redox behavior with both anodic and cathodic peaks. The anodic peak occurs around 0.44 V, and the cathodic peak is around 0.15 V, indicating a reversible redox process likely related to the Cu centers in the CuZIF framework [79]. Pt@CuZIF shows enhanced performance in both reduction and oxidation with cathodic peak of 40.36 mA around 0.07

V and anodic peak of 36.07 mA around 0.48 V making it an effective electrocatalyst [80–82], whereas Ru@CuZIF shows less cathodic current respond of 30.38 mA around 0.13 V and anodic current respond of 32.49 mA around 0.43 V. The use of electroless deposition of Pt and Ru enhances the electrochemical properties of CuZIF due to increment and shift of current density and potential [83, 84]. The peak currents for Pt@CuZIF are notably higher than both CuZIF and Ru@CuZIF, particularly at higher scan rates. This suggests that Pt enhances the electrocatalytic properties more effectively than Ru in this configuration, possibly due to its superior catalytic activity for redox processes involving copper or the CuZIF framework [85–87]. Cyclic voltammetry was employed to determine the highest occupied

molecular orbital (HOMO) and the lowest unoccupied molecular orbital (LUMO) using Eqs. 3 and 4 [88]:

$$E_{\text{HOMO}} = -[E_{\text{ox}} + 4.75] \text{ eV} \quad (3)$$

$$E_{\text{LUMO}} = -[E_{\text{red}} + 4.75] \text{ eV} \quad (4)$$

where E_{ox} is the oxidation onset potential and E_{red} is the reduction onset potential. The values of onset oxidation potentials were extrapolated to be 0.08, 0.25 and 0.21 V, and their corresponding HOMO energy level values were found to be -4.83, -5.00 and -4.96 eV, and the values of onset reduction potentials were extrapolated to be 0.47, 0.48 and 0.49 V, and their corresponding LUMO energy level values were found to be 4.76, 5.22 and 5.24 eV for CuZIF, Pt@CuZIF and Ru@CuZIF, respectively. The excellence chemical reactivity of the electrocatalyst can be attributed to its lower optical band gap, as materials with smaller band gaps tend to be less stable. The electrochemical band gap (E_g) was calculated from the difference between the HOMO and LUMO [70], and were found to be 0.38, 0.22 and 0.28 for CuZIF, Pt@CuZIF and Ru@CuZIF, respectively, as shown in Table 3.

The scan rate behavior and current response of the prepared materials, modified on the electrode surface, as shown in Fig. 4 (b-d), were analysed using cyclic voltammograms. The peak currents increase as the scan rate increases. This suggests that the process is diffusion-controlled, as peak current is proportional to the square root of the scan rate [70]. The influence of scan rates was used to investigate the electronic properties of the materials to understand the nature of the electrode processes occurring at the surface of bare [70], CuZIF, Pt@CuZIF and Ru@CuZIF materials. Figure 5 (a-h) shows scan rates studies for both cathodic and anodic peak currents to examine the electronic properties. In this study, we obtained the slope of the log current against log scan rate plot in Fig. 5 (a, b), which can indicate whether the reaction is diffusion-controlled or adsorption-controlled [65]. The relationship was found to be linear, with cathodic slopes of 0.67, 0.68, and 0.68, and anodic slopes of 0.72, 0.79, and 0.80 for CuZIF, Pt@CuZIF, and Ru@CuZIF, respectively. The cathodic slopes observed for CuZIF, Pt@CuZIF, and Ru@CuZIF, being close to the theoretical value of 0.5, suggest that the process is diffusion-controlled and the anodic slopes for these materials, which are near the theoretical

value of 1, indicate an adsorption-controlled process [70]. The plot of peak current against the square root of the scan rate in Fig. 5 (c, d) shows a strong linear relationship for both anodic and cathodic peak currents, indicating that the current is primarily governed by diffusion-controlled process [89, 90]. The diffusion coefficient (D) was determined using the Randles-Ševčík equation (Eq. 5), as outlined by [91]:

$$I = 2.678 \times 10^5 n^{3/2} A D^{1/2} v^{1/2} C \quad (5)$$

where I is the maximum peak current at the cathodic-anodic region, n is the number of electrons transferred within the redox process, A is the electroactive surface area, v is the scan rate, and C is the concentration of the analyte. The D values of CuZIF, Pt@CuZIF and Ru@CuZIF were found to be 1.34×10^{-5} , 1.54×10^{-5} and $8.67 \times 10^{-6} \text{ cm}^2 \text{ s}^{-1}$ for cathodic peak current and 1.87×10^{-5} , 1.51×10^{-5} and $1.23 \times 10^{-5} \text{ cm}^2 \text{ s}^{-1}$ for anodic peak current, respectively. This observation indicates that in the reduction process, Pt@CuZIF promotes faster electron diffusion [70], followed by Ru@CuZIF and then CuZIF. Conversely, in the oxidation process, CuZIF enhances electron diffusion more rapidly, followed by Pt@CuZIF and then Ru@CuZIF. Moreover, it was observed that the material not only experiences a diffusion process but can also adsorb onto the surface of the electrode [92]. This behavior can be explained by directly correlating the peak current with the surface coverage and the scan rate [55], as shown in Fig. 5 (a, b), using Eq. 6 [91]:

$$I_p = n^2 F^2 G A v / 4 R T \quad (6)$$

where I_p is the peak current from the cyclic voltammograms, Γ is the surface coverage, T is the absolute temperature, R is gas constant, and F is the Faradaic constant. It was observed that CuZIF, Pt@CuZIF and Ru@CuZIF covered 3.18×10^{-7} , 3.44×10^{-7} and $2.58 \times 10^{-7} \text{ mol cm}^{-2}$ in the reduction process and 3.79×10^{-7} , 3.39×10^{-7} and $3.06 \times 10^{-7} \text{ mol cm}^{-2}$ in the oxidation process, respectively, as shown in Table 4. These Γ values confirms the adsorption of the materials onto the surface of the nickel foam, indicating that the process is surface-controlled [93]. Determining the electrochemical active surface area (ECSA) is crucial for understanding the behavior of an electrocatalyst [94]. The capacitance double-layer (C_{dl}) is obtained by plotting the

Table 3 Electrochemical parameters of bare, CuZIF, Pt@CuZIF and Ru@CuZIF

Materials	I_c (A)	I_a (A)	I_a/I_c	$E_{1/2}^{\text{red}}$ (V)	$E_{1/2}^{\text{ox}}$ (V)	E_{HOMO} (eV)	E_{LUMO} (eV)	E_g (eV)
Bare	—	—	—	—	—	—	—	—
CuZIF	0.038	0.042	1.14	0.47	0.08	-4.83	-5.21	0.38
Pt@CuZIF	0.040	0.036	0.93	0.47	0.25	-5.00	-5.22	0.22
Ru@CuZIF	0.030	0.033	1.11	0.487	0.21	-4.96	-5.24	0.28

Fig. 5 Plot of **a** cathodic log of peak current against log of scan rate, **b** anodic log of peak current against log of scan rate, **c** cathodic peak current against square root of scan rate, **d** anodic peak current against square root of scan rate, **e** cathodic peak current against scan rate, **f** anodic peak current against scan rate, **g** cathodic change in peak current against scan rate and **h** electrochemical active surface area plot for CuZIF, Pt@CuZIF and Ru@CuZIF in 0.1 M KOH

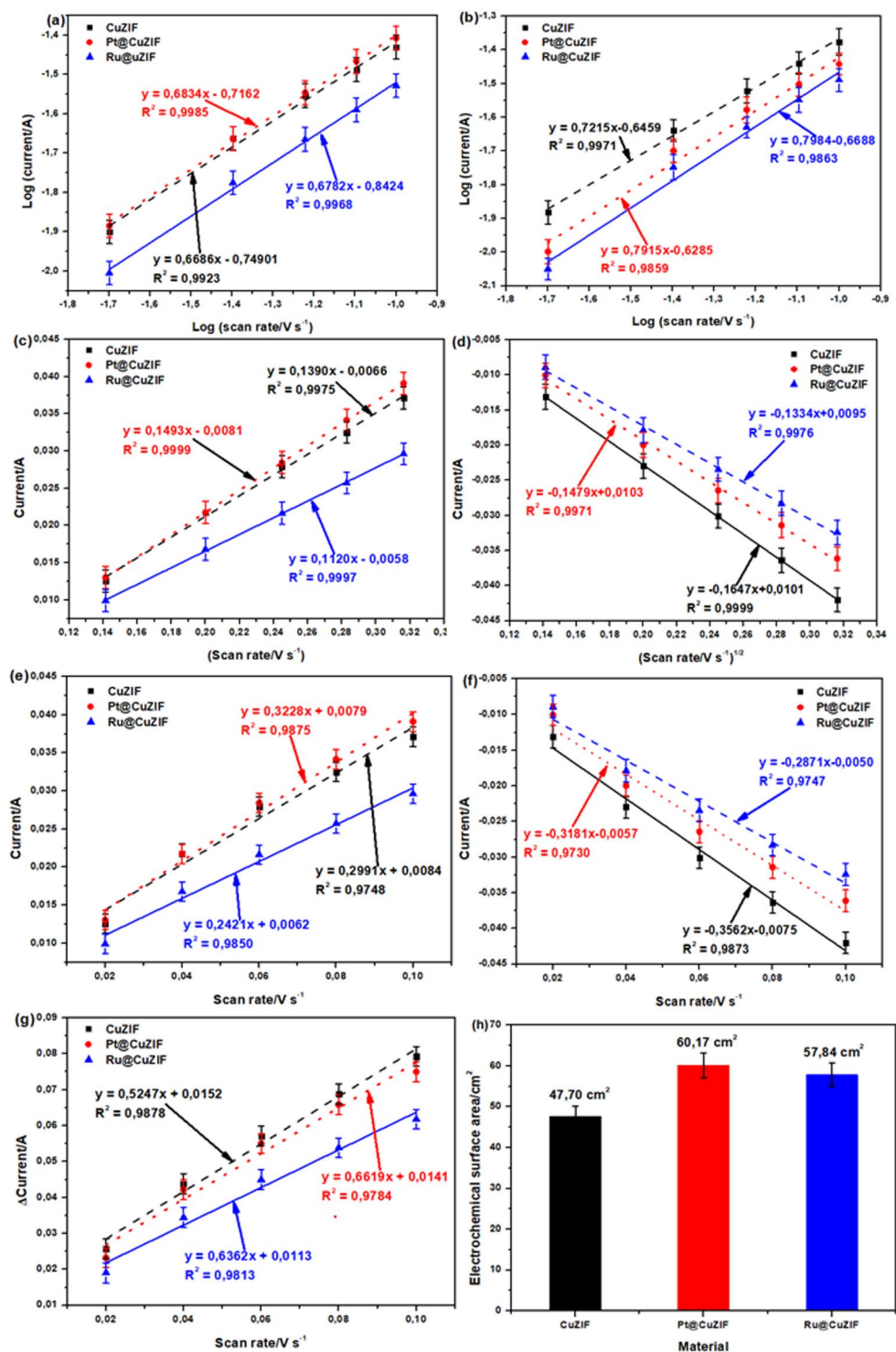


Table 4 Cathodic electrode parameters of CuZIF, Pt@CuZIF and Ru@CuZIF

Materials	Diffusion coefficient (cm ² s ⁻¹)		Surface coverage (x 10 ⁻⁷ mol cm ⁻²)		ECSA (cm ²)
	Cathode	Anode	Cathode	Anode	
CuZIF	1.34 × 10 ⁻⁵	1.87 × 10 ⁻⁵	3.18	3.79	47.70
Pt@CuZIF	1.54 × 10 ⁻⁵	1.51 × 10 ⁻⁵	3.44	3.39	60.17
Ru@CuZIF	8.67 × 10 ⁻⁶	1.23 × 10 ⁻⁵	2.58	3.06	57.84

differences in current against scan rate, which reflects the ECSA [55, 86] as shown in Fig. 5 (g), and their relationship depict direct proportionality. The C_{dl} values were found to be 1.05, 1.32, 1.27 mF cm⁻² for CuZIF, Pt@CuZIF and Ru@CuZIF, respectively. ECSA can be obtained from C_{dl} and it was calculated using Eq. 7 [95]:

$$\text{ECSA} = \text{C}_{\text{dl}}/\text{C}_s \quad (7)$$

where C_s is the specific capacitance (0.022 mF cm^{-2}) [96]. ECSA values were found to be 47.7, 60.17 and 57.84 cm^2 for CuZIF, Pt@CuZIF and Ru@CuZIF, respectively. This shows that Pt@CuZIF has more active sites available for adsorption and activation of reactants, which facilitates higher HER and OER followed by Ru@CuZIF then CuZIF.

3.3.2 Water electrolysis

The properties of CuZIF, Pt@CuZIF, and Ru@CuZIF were investigated in 0.1 M KOH at a scan rate of 10 mV s^{-1} . Figure 6 (a) shows the LSV curves, with HER occurring in the negative potential region and OER in the positive region. Pt@CuZIF exhibits the highest HER performance, with a lower overpotential of -0.77 V compared to CuZIF (-0.86 V) and Ru@CuZIF (-0.88 V) at 20 mA cm^{-2} . Figure 6 (b) presents the HER and OER Tafel plots at 10 mA cm^{-2} . For HER in alkaline media, commercial Pt/C is widely accepted as the benchmark and typically reaches 10 mA cm^{-2} at very small overpotentials of $45\text{--}60 \text{ mV}$ with Tafel slopes of $50\text{--}60 \text{ mV dec}^{-1}$ in 0.1 M KOH [96]. In comparison, Pt@CuZIF shows an overpotential of 345 mV , followed by CuZIF (363 mV) and Ru@CuZIF (412 mV) for HER. For OER, commercial IrO₂ and RuO₂ catalysts usually exhibit overpotentials of about $300\text{--}350 \text{ mV}$ at 10 mA cm^{-2} with Tafel slopes of $60\text{--}80 \text{ mV dec}^{-1}$ in alkaline media [97, 98]. By contrast, Ru@CuZIF achieves the lowest OER overpotential of 423 mV , followed by Pt@CuZIF (474 mV) and CuZIF (556 mV). This indicates that Pt incorporation into CuZIF enhances HER activity, whereas Ru incorporation improves OER performance. In comparison with other reported non-noble metal bifunctional catalysts, the prepared Pt@CuZIF and Ru@CuZIF exhibit competitive performance. For instance, Cu-ZIF-8 shows HER and OER overpotentials of 210 and 340 mV , respectively [39], while NiCo-ZIF/N-C achieves a HER and OER overpotentials of 165 and 295 mV , respectively, in 1.0 KOH [33]. Although some non-PGM catalysts outperform in either HER or OER individually, the Pt@CuZIF and Ru@CuZIF present balanced bifunctional activity, combining catalytic efficiency and enhanced conductivity through the synergistic interaction of Pt or Ru with the CuZIF framework. The electrochemical HER and OER behaviors of CuZIF, Pt@CuZIF, and Ru@CuZIF were further examined using Tafel plots to evaluate the rate-limiting steps [70]. Figures 6 (d-e) show Tafel plots derived from LSV data. The slopes of CuZIF, Pt@CuZIF, and Ru@CuZIF were 121.4 , 118.0 , and $121.3 \text{ mV dec}^{-1}$ for HER, and 124.5 , 118.5 , and $120.3 \text{ mV dec}^{-1}$ for OER, respectively, as summarised in Table 5. These results suggest that both HER and OER follow the

Volmer-Heyrovsky mechanism [99, 100]. In HER, the Volmer step ($\text{H}_2\text{O} + \text{e}^- \rightarrow \text{H}^* + \text{OH}^-$) involves proton adsorption on active sites, followed by the Heyrovsky step ($\text{H}^* + \text{H}_2\text{O} + \text{e}^- \rightarrow \text{H}_2 + \text{OH}^-$) [101]. Pt incorporation lowers the energy barrier for H^* adsorption-desorption, accelerating the Volmer step and enhancing HER kinetics [102]. For OER, the process proceeds via OH^- adsorption, formation of O^* and OOH^* intermediates, and subsequent O_2 release. Ru incorporation stabilizes oxygenated intermediates, particularly OOH^* , lowering the activation barrier of the rate-determining step and improving OER kinetics [103]. Thus, Pt@CuZIF demonstrates the fastest HER kinetics (118 mV dec^{-1}), while Ru@CuZIF exhibits the most favorable OER kinetics ($118.5 \text{ mV dec}^{-1}$). Durability, amount of gas produced and Faradaic efficiency (FE) were further evaluated using chronoamperometry (CA) at 0.35 V applied potential for OER as the example. The CA curves were presented in Fig. 6 (f). CuZIF exhibited the highest initial current of 34 mA , but the current rapidly decayed to 12 mA , reflecting poor structural stability under alkaline conditions, in line with earlier reports on ZIF instability in long-term cycling [104–106]. In contrast, Pt@CuZIF and Ru@CuZIF displayed lower initial currents of $11\text{--}12 \text{ mA}$ but maintained stable performance around $2\text{--}3 \text{ mA}$ throughout the test, confirming their superior durability. The enhanced stability of Pt@CuZIF can be attributed to strong Pt-N coordination within the ZIF framework, which suppresses structural collapse and facilitates charge transfer [35, 82], while Ru incorporation stabilizes oxygenated intermediates during OER, reducing degradation of the CuZIF host [103, 108]. The amount of O_2 produced was determined using the Faraday's law as outlined in Eq. 8 [70]:

$$\text{O}_2 \text{ production rate} = 60I_{\text{CA}}/\text{nFm} \quad (8)$$

where I_{CA} is the current from CA, n is the number of electron transfer (4 mol), m is the mass of electrocatalyst and F is the Faradaic constant (96500 C/mol). Accordingly, CuZIF electrocatalyst was able to evolve 2.81 mol/g/min oxygen. In comparison the amounts of produced oxygen for Pt@CuZIF and Ru@CuZIF were calculated as 0.77 and 1.07 mol/g/min , respectively. In order to determine the FE of the electrocatalyst, the following Eq. 9 was used as adopted from Khaligh et al. [109]:

$$\% \text{FE} = (I_{\text{CA}}/I_{\text{LSV}}) \times 100\% \quad (9)$$

where I_{LSV} is the current of LSV as the potential which CA experiment was performed. The %FE values were calculated to be 156 , 39 and 68% for CuZIF, Pt@CuZIF and Ru@CuZIF, respectively. It was seen that the CA of CuZIF achieved higher currents and detect faster reactions than

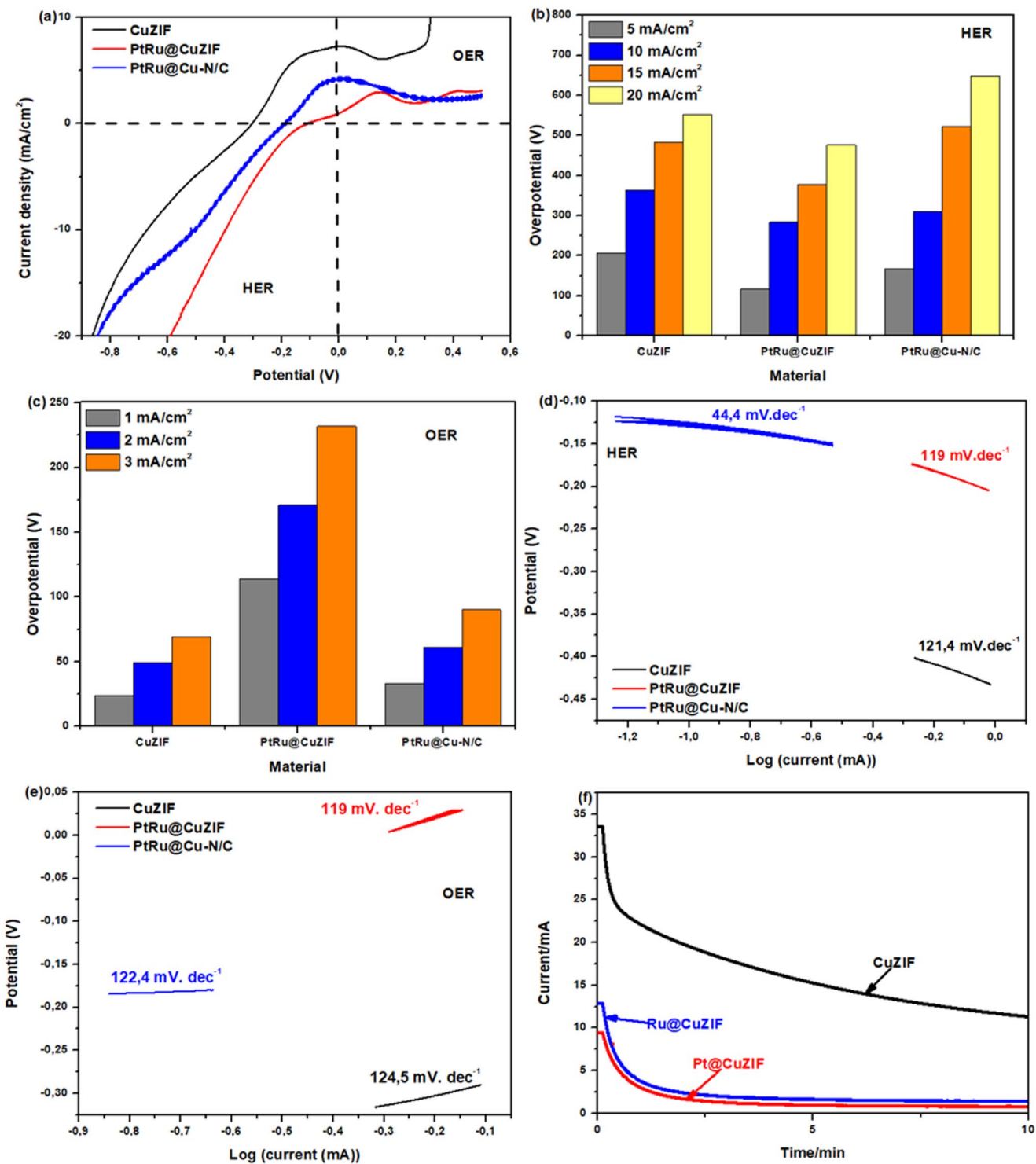


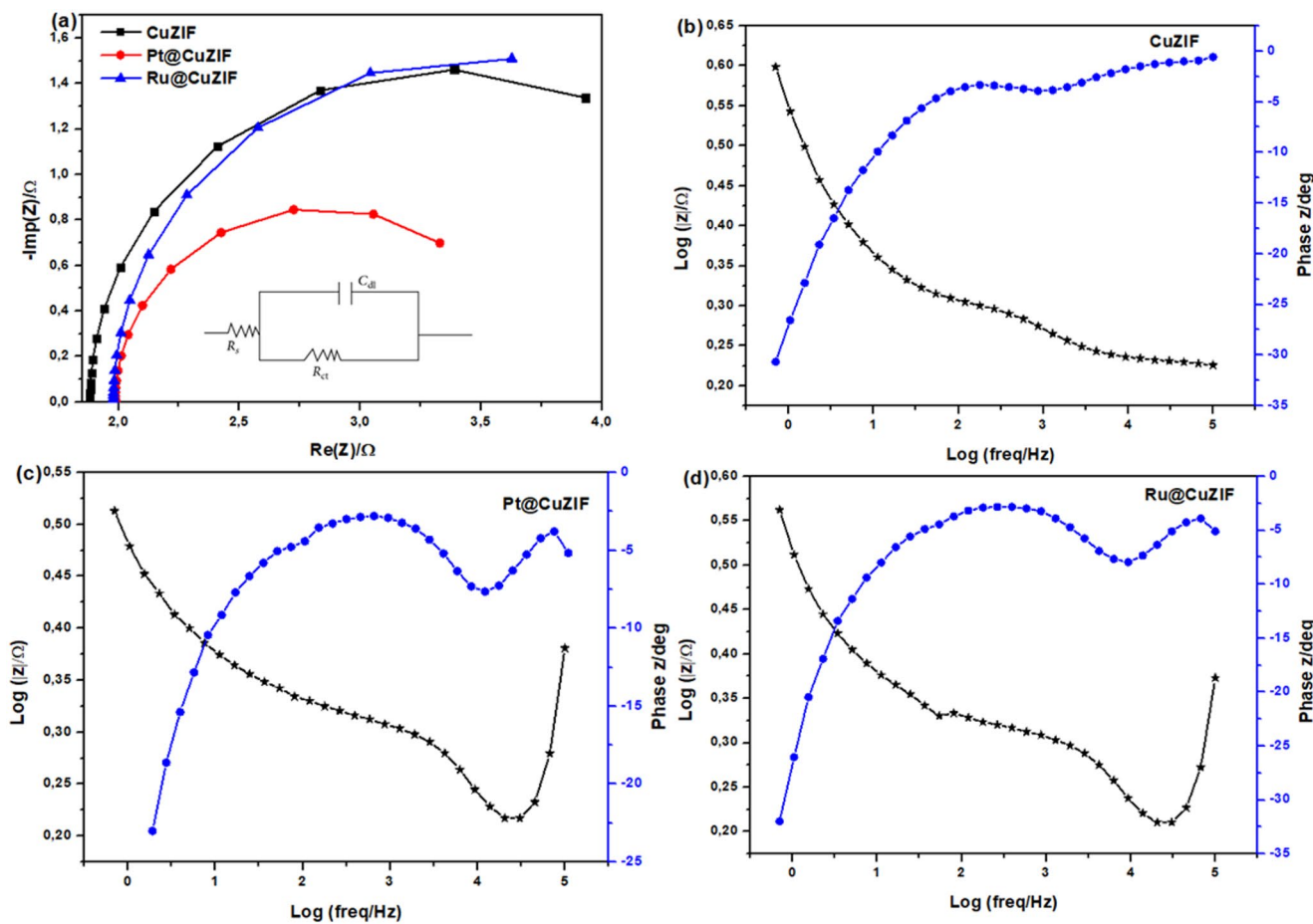
Fig. 6 **a** LSV curve of CuZIF, Pt@CuZIF and Ru@CuZIF and its corresponding overpotentials, **b** at 5, 10, 15 and 20 mA cm^{-2} for HER, **c** 5, 10, 15, 20 and 25 mA cm^{-2} for OER, **d** and **e** Tafel plots of CuZIF, Pt@CuZIF and Ru@CuZIF for HER and OER, respectively, and **f** CA plots of CuZIF, Pt@CuZIF and Ru@CuZIF in 0.1 M KOH

LSV because it applies a single potential step, allowing for shorter sampling times and greater sensitivity to short-term processes [110]. CA and LSV reveals the adverse impact of

high carbonate buffer concentrations on anode performance in microbial fuel cells [111].

Table 5 Comparative analysis of HER and OER performance

Materials	KOH (M)	HER			OER			References
		η (mV)	-b (mV dec ⁻¹)	α	η (mV)	-b (mV dec ⁻¹)	α	
CuZIF	0.1	363	121,4	0.52	556	124,5	0.53	[This work]
Pt@CuZIF	0.1	345	118	0.51	474	118,5	0.51	[This work]
Ru@CuZIF	0.1	412	121,3	0.52	423	120,3	0.52	[This work]
Cu-ZIF-8	1.0	210	65	—	340	72	—	[98]
NiCo-ZIF/N-C	1.0	165	49	—	295	61	—	[100]
ZIF-67	1.0	440	193	—	—	—	—	[104]
Cu-N-SC-1100	0.1	—	—	—	1254	75,3	—	[105]
ZIF-8@ZIF-67@POM	1.0	—	—	—	490	88	—	[106]
ZIF-67-C/FeOOH	1.0	—	—	—	285	40	—	[107]
Co@N-C (derived from ZIF-67)	1.0	175	52	—	310	68	—	[108]

**Fig. 7** a EIS plots of CuZIF, Pt@CuZIF and Ru@CuZIF and Bode plot of b CuZIF, c Pt@CuZIF and d Ru@CuZIF in 0.1 M KOH

3.3.3 Electrochemical impedance spectroscopy

EIS measurements were conducted using the standard three-electrode system to evaluate the charge transfer kinetics in these samples. The semicircle diameter is regarded as an indicator of charge transfer at the electrode/electrolyte interface during the OER and HER [69]. Figure 7 (a) shows the Nyquist plots of CuZIF, Pt@CuZIF and Ru@CuZIF. Pt@CuZIF shows a smaller semicircle diameter compared to

CuZIF and Ru@CuZIF suggesting high charge transfer efficiency [112–114]. This indicates that the interaction of Pt on CuZIF enhances the electron transfer. Ru@CuZIF has a similar curve as CuZIF but shows higher impedance values. While Ru@CuZIF also improves conductivity by reducing charge transfer resistance (R_{ct}) due to the interaction of Ru on CuZIF, Pt@CuZIF appears to perform much better compared to CuZIF and Ru@CuZIF. The R_{ct} values were found to be 2.05, 1.32 and 1.64 Ω for CuZIF, Pt@CuZIF and Ru@

CuZIF, respectively. The Bode plots for CuZIF, Pt@CuZIF and Ru@CuZIF, as displayed in Fig. 7 (b-d), are used to estimate the electron lifetime (τ) and conductivity (σ) for these materials. The σ was calculated using Eq. 10 [114, 115]:

$$\sigma = t/R_{ct}A \quad (10)$$

where t is the thickness of an electrode (0.16 cm) and A is the area of the substrate. The σ values of CuZIF, Pt@CuZIF and Ru@CuZIF was found to be 0.16, 0.24 and 0.20 S cm^{-1} , respectively. Pt@CuZIF shows the highest σ as compared to Ru@CuZIF and CuZIF. This suggest that the incorporation of Pt on CuZIF enhances the σ value. The R_{ct} was used to calculate the exchange current density (j_o) where $j_o = i_o/A$ and the apparent heterogeneous electron transfer rate constant (k^o) following the Eqs. 11 and 12 [116]:

$$i_o = RT/nFR_{ct} \quad (11)$$

$$k^o = i_o/nFAC = j_o/nFC \quad (12)$$

where n is the number of electron transfer, R is molar gas constant, T is the temperature, F is Faradaic constant, and C is the concentration of electrolyte. The j_o and k^o reveal the intrinsic rate of transfer of electrons between the electrode and the electrolyte. The calculated exchange current densities as shown in Table 6, were found to be 1.25×10^{-2} , 1.95×10^{-2} and $1.57 \times 10^{-2}\text{ mA cm}^{-2}$ for CuZIF, Pt@CuZIF and Ru@CuZIF, respectively. The estimated k^o values as given in Table 6, were obtained to be 1.30×10^{-5} , 2.02×10^{-5} and $1.62 \times 10^{-5}\text{ cm s}^{-1}$ for CuZIF, Pt@CuZIF and Ru@CuZIF, respectively. The most significant values of j_o and k^o related to Pt@CuZIF indicate faster electron transfer process [116].

The τ was calculated from the Bode plots using Eq. 13 [95]:

$$\tau = 1/(2\pi f_{max}) \quad (13)$$

where f_{max} is the maximum peak frequency. The f_{max} was estimated to be around 47.8, 31.4, 32.8 ° and their corresponding τ values were found to be 3.32, 5.06, 4.85 ms for CuZIF, Pt@CuZIF and Ru@CuZIF, respectively. Pt@CuZIF shows the longest τ compared to Ru@CuZIF and CuZIF. The C_{dl} was also determined from Bode plots to

predict the electrical energy storage via electrical double layer effect and was calculated using Eq. 14 [93, 117]:

$$C_{dl} = 1/(2\pi f_{max})R_{ct} \quad (14)$$

Table 6 shows the summarised parameters obtained. The C_{dl} values were found to be 1.6, 3.84 and 2.96 mF for CuZIF, Pt@CuZIF and Ru@CuZIF, respectively. Pt@CuZIF shows the highest C_{dl} compared to Ru@CuZIF and CuZIF from the both EIS and CV. This suggest that Pt@CuZIF have enhanced energy storage capability which can increase the material's surface charge storage capacity and electrochemical active surface area for EIS and CV, respectively [118].

3.3.4 Hydrogen fuel cell

The performance of the synthesized electrocatalysts in water splitting fuel cell was evaluated in the closed system of single electrochemical cell in 0.1 M KOH. The CV was used to generate H_2/O_2 as shown in Fig. 8 (a-c) for CuZIF, Pt@CuZIF and Ru@CuZIF, respectively. The figures reveal both reduction and oxidation peaks for H_2 and O_2 evolution and evidence for the saturation of gas bubbles on the counter and working electrodes were also observed as given in the Fig. 8 (d). The 10 CV cycles were maintained and no observation of the additional/decreased cathodic/anodic peak current. Furthermore, the scan rate dependent was evaluated and given in Fig. 9 (a-c) for CuZIF, Pt@CuZIF and Ru@CuZIF, respectively. They showed the increased in current with increase in the scan rates and more gas bubbles were observed at the low scan rates. This behaviour was observed in the work of Chen et al. [119] for the hydrogen bubble formation at hydrogen-insertion electrodes. The dynamics of gas bubbles on electrode surfaces has been widely studied using a variety of technologies [120–122].

After the cycles, the polarization current-voltage (I-V) curves in Fig. 10 (a) were also investigated for the continuation of water splitting to generate more gases. The I-V curves at zero current density started with the open circuit voltage (OCV) of 0.75, 0.73 and 0.71 V for the CuZIF, Pt@CuZIF and Ru@CuZIF, respectively. The observed OCV was due to the presence of H_2/O_2 reaction. The cell was then charged to 2 V using a constant current of 1 mAh current (3 A g^{-1}), during which protons and electrons were generated. The generation process exhibits a linear voltage-current density curve in CuZIF and Pt@CuZIF and quasi-linear

Table 6 The EIS Nyquist parameters of the prepared electrocatalyst

Materials	R_{ct} (Ω)	R_s (Ω)	σ (S cm^{-1})	j_o ($\times 10^{-2}\text{ mA cm}^{-2}$)	k^o ($\times 10^{-5}\text{ cm s}^{-1}$)	F_{max} (°)	τ (ms)	C_{dl} (mF)
CuZIF	2.05	4.81	0.16	1.25	1.30	47.8	3.32	1.62
Pt@CuZIF	1.32	3.09	0.24	1.95	2.02	31.4	5.06	3.84
Ru@CuZIF	1.64	3.27	0.20	1.57	1.62	32.8	4.85	2.96

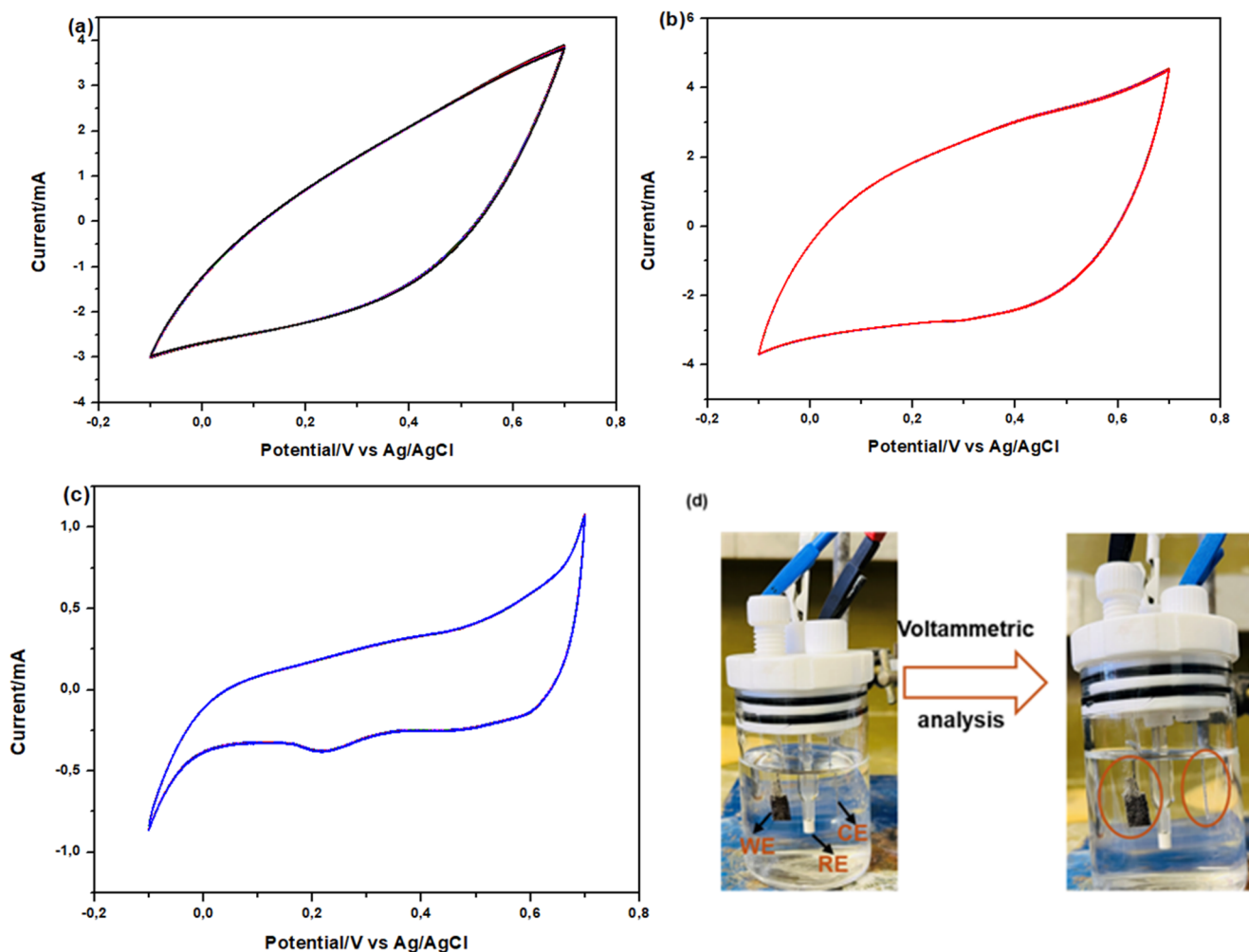


Fig. 8 CV measurements achieved 10 cycles for **a** CuZIF, **b** Pt@CuZIF, **c** Ru@CuZIF at 100 mV s^{-1} in 0.1 M KOH , and **d** photographic image of single electrochemical cell showing the generation of H_2/O_2 gases during voltammetric analysis

voltage-current density curve in Ru@CuZIF. There was an increased in current with increase in potential. The CuZIF produced a current density of 29.47 A g^{-1} at 2 V , while at the same condition, Pt@CuZIF showed 33.37 A g^{-1} current density and 24.43 A g^{-1} for Ru@CuZIF. This was also supported by the power density curves in Fig. 10 (b).

Figure 10 (c) shows galvanostatic discharge behavior of CuZIF, Pt@CuZIF and Ru@CuZIF in fuel cell at 3 mA current, potential range of 0 to 5 V and discharge resistance of 21Ω . The potential degraded was calculated from the difference between the highest potential at 0 s and the lowest potential at 1200 s . The highest potentials were observed to be 0.75 , 0.78 and 0.70 V , the lowest potentials were observed to be 0.43 , 0.65 and 0.53 V , and the potentials consumed were found to be 0.32 , 0.13 and 0.17 V for CuZIF, Pt@CuZIF and Ru@CuZIF, respectively. Based on the results obtained, Pt@CuZIF shows excellent performance and longevity, likely due to higher activity and better resistance to degradation during hydrogen oxidation and the

interaction of Pt on CuZIF. CuZIF shows the highest initial potential compared to Pt@CuZIF and Ru@CuZIF but degrades faster, indicating lower catalytic activity and durability [123]. This highlights Pt@CuZIF as the most effective catalyst for HFCs. The specific capacity (Q) and specific capacitance (C_s) of the CuZIF, Pt@CuZIF and Ru@CuZIF were calculated from the discharge curves using Eqs. 15 and 16 [124, 125], respectively:

$$Q = I \times t / m \quad (15)$$

$$C_s = 3.6 * Q / \Delta V \quad (16)$$

where I is current, ΔV is the discharged potential, m is the mass of active material and t is the discharge time. The Q values were obtained to be 529 , 526 , and 535 mAh g^{-1} for the CuZIF, Pt@CuZIF and Ru@CuZIF, respectively. The obtained Q values were converted to the C_s and found to be 5.95 , 14.57 and 11.32 F g^{-1} for the CuZIF, Pt@CuZIF

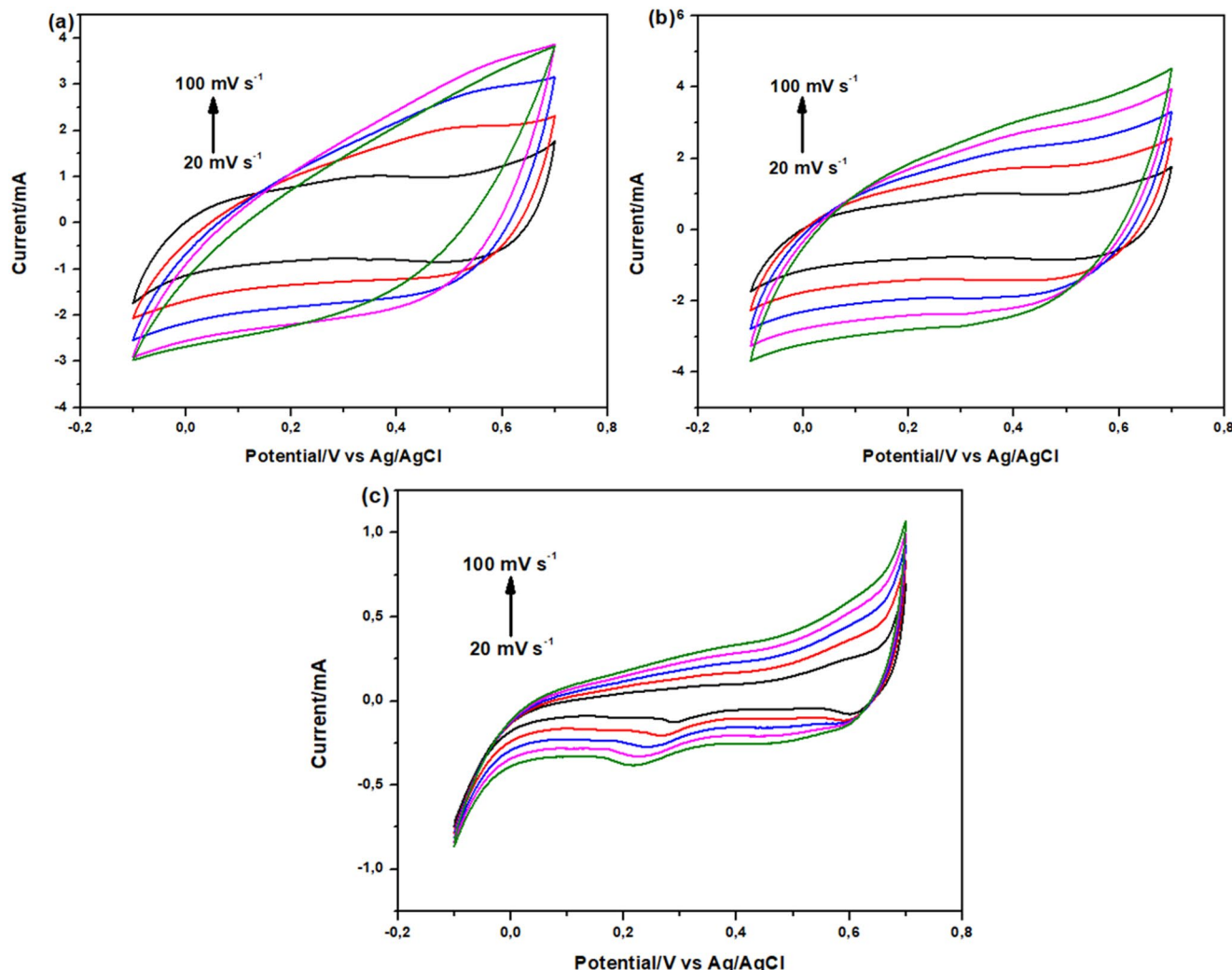


Fig. 9 CV measurements achieved 10 cycles for **a** CuZIF, **b** Pt@CuZIF and **c** Ru@CuZIF at 20–100 mV s⁻¹ in 0.1 M KOH

and Ru@CuZIF, respectively. Pt@CuZIF shows the highest C_s followed by Ru@CuZIF then CuZIF. This indicates that the incorporation of Pt and Ru on CuZIF enhances the electrical conductivity and introducing additional active sites, enabling good discharge capacity. The energy density (E_d) was calculated from C_s to know the amount of energy released in 1200 s using Eq. 17 [124, 125]:

$$E_d = \int IV / mdt \quad (17)$$

The parameters are summarized in Table 7. The E_d was found to be 169.31, 68.42 and 90.91 Wh kg⁻¹ for the CuZIF, Pt@CuZIF and Ru@CuZIF, respectively, which were higher than ZIF-67/rGO//ZIF-67/rGO [126]. The E_d obtained was used to calculate power density (P_d) using Eq. 18 [124, 125]:

$$P_d = E_d / t \quad (18)$$

The P_d values were found to be 507.94, 205.26, and 272.73 W kg⁻¹ for CuZIF, Pt@CuZIF and Ru@CuZIF, respectively. Based on the results obtained, it was observed that the incorporation of Pt and Ru onto CuZIF deliver to enough P_d at low discharge rate suitable for H₂/O₂ fuel cell.

4 Conclusion

In this study, CuZIF, Pt@CuZIF, and Ru@CuZIF electrocatalysts were successfully synthesized via electroless plating and systematically investigated for their structural, electrochemical, and fuel cell properties. Structural analysis confirmed the incorporation of Pt and Ru into the CuZIF framework without compromising crystallinity, while morphological studies revealed uniform dispersion of metallic nanoparticles. Electrochemical characterisation

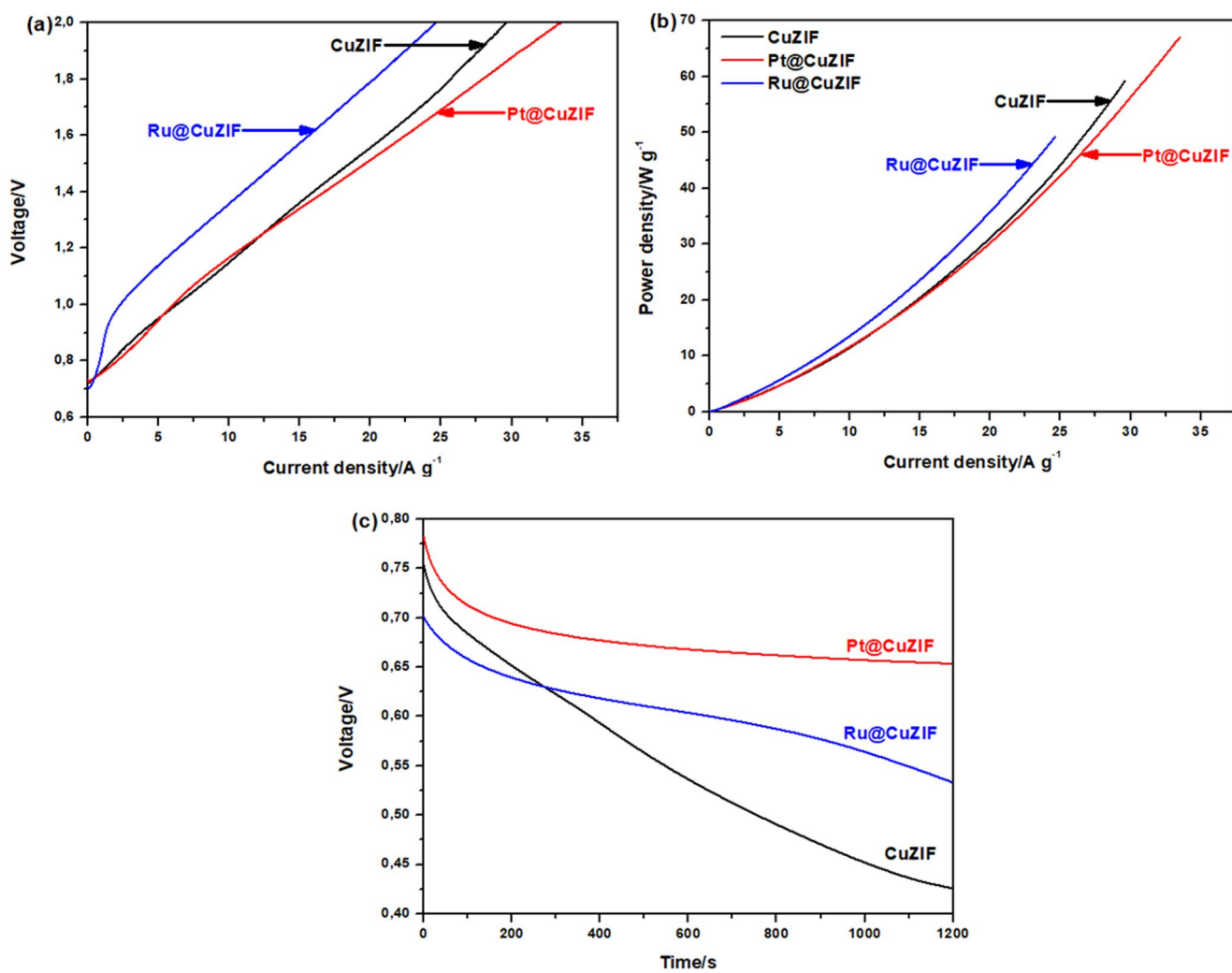


Fig. 10 **a** I–V curve, **b** power density and **c** galvanostatic discharge plot of CuZIF, Pt@CuZIF and Ru@CuZIF in 0.1 M KOH

Table 7 Electrochemical parameters for fuel cell

Materials	Voltage (V)	Active mass (mg)	Specific capacitance (F g ⁻¹)	Energy density (Wh kg ⁻¹)	Power density (W kg ⁻¹)	References
CuZIF	0.32	1.87	5.95	169.31	507.94	[This work]
Pt@CuZIF	0.13	1.90	14.57	68.42	205.26	[This work]
Ru@CuZIF	0.17	1.89	11.32	90.91	272.73	[This work]
ZIF-67/rGO//ZIF-67/rGO	1.5	—	—	25.5	2700	[126]
ZIF-8/Carbon Composite	—	—	—	43.7	900	[127]
NiCo-ZIF@CNT	—	—	—	45.4	800	[128]
NiCoFe-LDH@ZIF-67	—	—	—	69.6	750	[129]

demonstrated that Pt@CuZIF exhibited the highest HER activity with a low overpotential of 345 mV, Tafel slope of 118 mV dec⁻¹, and superior conductivity of 0.24 S cm⁻¹, indicating fast charge-transfer kinetics. Ru@CuZIF showed improved OER performance with an overpotential of 423 mV and enhanced stabilization of oxygen intermediates. EIS analysis further confirmed that Pt@CuZIF achieved the lowest R_{ct} (1.32 Ω) and highest exchange current density

of 1.95×10^{-2} mA cm⁻², underscoring its superior electron transfer ability. In HFC studies, Pt@CuZIF demonstrated excellent discharge stability of 0.13 V degradation, energy density of 68.42 Wh kg⁻¹, and power density of 205.26 W kg⁻¹, outperforming CuZIF and Ru@CuZIF. Although CuZIF initially displayed higher voltage, its rapid degradation highlighted poor durability, whereas Pt@CuZIF maintained longer operational stability. These results confirm

Pt@CuZIF as the most efficient trifunctional catalyst for HER, OER, and HFC applications among the tested materials. Although Pt is relatively expensive, the Pt loading in Pt@CuZIF is very low (1.87 wt% from EDX analysis, which drastically reduces the overall cost compared to conventional bulk Pt or Pt/C catalysts. At this minimal loading, Pt still provides significant improvements in HER and HFC performance by lowering overpotential, enhancing R_{ct} , and maintaining higher stability during cycling. In fact, the efficiency gain per unit mass of Pt is considerably higher in Pt@CuZIF because the CuZIF support ensures maximum dispersion and utilization of Pt active sites. Thus, the catalyst achieves a cost-to-performance balance, where the amount of noble metal is minimized while still attaining competitive activity and durability. Future work should focus on durability testing under real operating conditions, reducing noble metal content, and exploring synergistic bimetallic or heteroatom-doped MOFs to advance the commercial viability of hydrogen energy technologies.

Acknowledgements The authors would like to thank the financial support from the National Research Foundation (NRF) under the Thuthuka (UID No. 2204264960) of Dr Maponya TC, the Competitive Support for Unrated Researchers (UID No. 138085) programmes and DSI-NRF SARChI Chair (UID No. 150531) of Prof Modibane KD.

Author contributions Conceptualization, J.R., and K.D.M.; Performed the experiments, T.M.; Formal analysis, T.M., G.R.M and K.D.M.; Funding acquisition, K.D.M.; Project administration, G.R.M., K.E.R and K.D.M.; Writing—Original draft, T.M and K.E.R., All authors have read and agreed to the published version of the manuscript.

Funding The authors would like to thank the financial support from the National Research Foundation (NRF) under the Thuthuka (UID No. 2204264960) of Dr Maponya TC, the Competitive Support for Unrated Researchers (UID No. 138085) programmes and DSI-NRF SARChI Chair (UID No. 150531) of Prof Modibane KD.

Data availability Data will be made available on request from the corresponding author, Prof KD Modibane.

Declarations

Competing interests The authors declare no competing interests.

References

- Shen M, Huang W, Chen M, Song B, Zeng G, Zhang Y (2020) (Micro) plastic crisis: un-ignorable contribution to global greenhouse gas emissions and climate change. *J Clean Prod* 254:120138
- Singh S, Jain S, Venkateswaran PS, Tiwari AK, Nouni MR, Pandey JK, Goel S (2015) Hydrogen: a sustainable fuel for future of the transport sector. *Renew Sustain Energy Rev* 51:623–633
- Coutts D (2007) Ensuring adequate safety when using hydrogen as a fuel
- Vielstich W, Gasteiger HA, Yokokawa H (2009) Handbook of Fuel Cells: Advances in Electrocatalysis, Materials, Diagnostics and Durability, Volumes 5 and 6. John Wiley & Sons
- Xu K, Liu G, Xu X, Wang Z, Liu G, Liu F, Zhang Y, Zhou Y, Zou Y, Pei S (2024) Cerium based metal-organic framework as the efficient radical quencher for proton exchange membrane fuel cells. *J Membr Sci* 699:122641
- Li Y, Wei X, Chen L, Shi J (2021) Electrocatalytic hydrogen production trilogy. *Angew Chem Int Ed* 60(36):19550–19571
- Kim Y, Yang H (2025) Hydrogen purity: influence of production methods, purification techniques, and analytical approaches. *Energies* 18(3):741
- Liu T, Chen C, Pu Z, Huang Q, Zhang X, Al-Enizi AM, Nafady A, Huang S, Chen D, Mu S (2024) Non-noble-metal-based electrocatalysts for acidic oxygen evolution reaction: recent progress, challenges, and perspectives. *Small* 20(48):2405399
- Hussain M, El Maaty LA, Alomar MA, Ali M, Abdullah M, Aman S, Farid HMT (2024) Improvement of spinel OER electrochemical property by doping strategy for water splitting. *Appl Phys A Mater Sci Process* 130(8):554
- Gouadria S, Abdillah M, Ahmad Z, John P, Nisa MU, Manzoor S, Aman S, Ashiq MN, Ghori MI (2023) Development of bifunctional mo doped ZnAl₂O₄ spinel nanorods array directly grown on carbon fiber for supercapacitor and OER application. *Ceram Int* 49(3):4281–4289
- Aman S, Ahmad N, Tahir MB, Alanazi MM, Abdelmohsen SA, Khosa RY, Farid HMT (2023) Understanding the spatial configurations of Sm₂O₃ in NiO interfaces Embedded-Loaded for Electrocatalytic OER process. *Surf Interfaces* 38:102857
- Al-Yousef HA, El Maati LA, Alomar M, Farid HMT, Eman S, Bahlool T (2025) A novel FeAl₂O₃/g-CN (FAO/g-CN) material as an electrocatalyst with promising potential for OER. *Diamond Relat Mater* 154:112157
- Alburaih HA, Manzoor S, Abdullah M, Ashiq MN, Aman S, Trukhanov SV, Zubair TI, Sun Z, Taha TA, Trukhanov AV (2023) Electro-oxidation reconstitution of aluminium copper MOF-derived metal oxyhydroxides for a robust OER process. *RSC Adv* 13(13):8736–8742
- Li L, Tang X, Wu B, Huang B, Yuan K, Chen Y (2024) Advanced architectures of air electrodes in Zinc–Air batteries and hydrogen fuel cells. *Adv Mater* 36(13):2308326
- Zatoń M, Rozière J, Jones DJ (2017) Current understanding of chemical degradation mechanisms of perfluorosulfonic acid membranes and their mitigation strategies: a review. *Sustain Energy Fuels* 1(3):409–438
- Peighambardoust SJ, Rowshanzamir S, Amjadi M (2010) Review of the proton exchange membranes for fuel cell applications. *Int J Hydrog Energy* 35(17):9349–9384
- Wang C, Wang S, Peng L, Zhang J, Shao Z, Huang J, Sun C, Ouyang M, He X (2016) Recent progress on the key materials and components for proton exchange membrane fuel cells in vehicle applications. *Energies* 9(8):603
- Kusoglu A, Weber AZ (2017) New insights into perfluorinated sulfonic-acid ionomers. *Chem Rev* 117(3):987–1104
- Bessler WG, Vogler M, Störmer H, Gerthsen D, Utz A, Weber A, Ivers-Tiffée E (2010) Model anodes and anode models for understanding the mechanism of hydrogen oxidation in solid oxide fuel cells. *Phys Chem Chem Phys* 12(42):13888–13903
- Cheng F, Chen J (2012) Metal-air batteries: from oxygen reduction electrochemistry to cathode catalysts. *Chem Soc Rev* 41(6):2172–2192
- Mani-Lata C, Hussakan C, Panomsuwan G (2020) Fast and facile synthesis of Pt nanoparticles supported on ketjen black by solution plasma sputtering as bifunctional HER/ORR catalysts. *J Compos Sci* 4(3):121

22. Ajdari FB, Kowsari E, Shahrok MN, Ehsani A, Kiaei Z, Torkzaban H, Ershadi M, Eshkalak SK, Haddadi-Asl V, Chinnappan A, Ramakrishna S (2020) A review on the field patents and recent developments over the application of metal organic frameworks (MOFs) in supercapacitors. *Coord Chem Rev* 422:213441
23. Zhu B, Zou R, Xu Q (2018) Metal–organic framework based catalysts for hydrogen evolution. *Adv Energy Mater* 8(24):1801193
24. Yancey AD, Terian SJ, Shaw BJ, Bish TM, Corbin DR, Shiflett MB (2022) A review of fluorocarbon sorption on porous materials. *Microporous Mesoporous Mater* 331:111654
25. Liu Y, Chen L, Yang L, Lan T, Wang H, Hu C, Han X, Liu Q, Chen J, Feng Z, Cui X (2024) Porous framework materials for energy & environment relevant applications: a systematic review. *Green Energy Environ* 9(2):217–310
26. Ji Z, Wang H, Canossa S, Wuttke S, Yaghi OM (2020) Pore chemistry of metal–organic frameworks. *Adv Funct Mater* 30(41):2000238
27. Zhu L, Li Y, Ye P, Zhao J, Liu J, Lei J, Wang L, Xue R (2023) Ultra-stable, highly proton conductive, and self-healing proton exchange membranes based on molecule intercalation technique and noncovalent assembly nanostructure. *Adv Funct Mater* 33(10):2210453
28. Liu Q, Li Z, Wang D, Li Z, Peng X, Liu C, Zheng P (2020) Metal organic frameworks modified proton exchange membranes for fuel cells. *Front Chem* 8:694
29. Fan L, Kang Z, Li M, Sun D (2021) Recent progress in pristine MOF-based catalysts for electrochemical hydrogen evolution, oxygen evolution and oxygen reduction. *Dalton Trans* 50(17):5732–5753
30. Wu H, Wang J, Jin W, Wu Z (2020) Recent development of two-dimensional metal–organic framework derived electrocatalysts for hydrogen and oxygen electrocatalysis. *Nanoscale* 12(36):18497–18522
31. Li S, Tang D, Jing X (2024) Metal-organic framework-based self-supported electrodes for oxygen evolution reaction. *Chemical Synthesis* 4(4):N-A
32. Huang H, Zhao Y, Bai Y, Li F, Zhang Y, Chen Y (2020) Conductive metal–organic frameworks with extra metallic sites as an efficient electrocatalyst for the hydrogen evolution reaction. *Adv Sci* 7(9):2000012
33. Li FL, Shao Q, Huang X, Lang JP (2018) Nanoscale trimetallic metal–organic frameworks enable efficient oxygen evolution electrocatalysis. *Angew Chem* 130(7):1906–1910
34. Gidi L, Amalraj J, Tenreiro C, Ramírez G (2023) Recent progress, trends, and new challenges in the electrochemical production of green hydrogen coupled to selective electrooxidation of 5-hydroxymethylfurfural (HMF). *RSC Adv* 13(40):28307–28336
35. Makhafola MD, Balogun SA, Modibane KD (2024) A comprehensive review of bimetallic nanoparticle–graphene oxide and bimetallic nanoparticle–metal–organic framework nanocomposites as photo-, electro-, and photoelectrocatalysts for hydrogen evolution reaction. *Energies* 17(7):1646
36. Jung H, Karmakar A, Adhikari A, Patel R, Kundu S (2022) Graphene-based materials as electrocatalysts for the oxygen evolution reaction: a review. *Sustain Energy Fuels* 6(3):640–663
37. Yusran Y, Fang Q, Valtchev V (2020) Electroactive covalent organic frameworks: design, synthesis, and applications. *Adv Mater* 32(44):2002038
38. Liu J, Goetjen TA, Wang Q, Knapp JG, Wasson MC, Yang Y, Syed ZH, Delferro M, Notestein JM, Farha OK, Hupp JT (2022) MOF-enabled confinement and related effects for chemical catalyst presentation and utilization. *Chem Soc Rev* 51(3):1045–1097
39. Parkash A (2020) Copper doped zeolitic imidazole frameworks (ZIF-8): a new generation of single-atom catalyst for oxygen reduction reaction in alkaline media. *J Electrochem Soc* 167(15):155504
40. Ohno I (2010) Electroless deposition of palladium and platinum. *Modern electroplating*. pp 477–482
41. Dojčinović MP, Stojković Simatović I, Nikolić MV (2024) Supercapacitor electrodes: is nickel foam the right substrate for active materials? *Materials* 17(6):1292
42. Mashao G, Ramohlolae KE, Mdluli SB, Monama GR, Hato MJ, Makgopa K, Molapo KM, Ramoroka ME, Iwuoha EI, Modibane KD (2019) Zinc-based zeolitic benzimidazolate framework/poly-aniline nanocomposite for electrochemical sensing of hydrogen gas. *Mater Chem Phys* 230:287–298
43. Huang Y, Liu D, Liu Z, Zhong C (2016) Synthesis of zeolitic imidazolate framework membrane using temperature-switching synthesis strategy for gas separation. *Ind Eng Chem Res* 55(26):7164–7170
44. Nakamoto K (2009) Infrared and Raman spectra of inorganic and coordination compounds, part B: applications in coordination, organometallic, and bioinorganic chemistry. John Wiley & Sons
45. Hidayati LN, Aulia F, Napitupulu SU, Adhyaksa GWP, Dahnum D (2024) Synthesize and characterization of Pt-supported Co-ZIF for catalytic hydrocracking and hydroisomerization of n-Hexadecane. *Bull Chem React Eng Catal* 19(1):171–180
46. Liu J, He J, Wang L, Li R, Chen P, Rao X, Deng L, Rong L, Lei J (2016) NiO-PTA supported on ZIF-8 as a highly effective catalyst for hydrocracking of *Jatropha* oil. *Sci Rep* 6(1):23667
47. Hadjiivanov KI, Panayotov DA, Mihaylov MY, Ivanova EZ, Chakarova KK, Andonova SM, Drenchev NL (2020) Power of infrared and Raman spectroscopies to characterize metal-organic frameworks and investigate their interaction with guest molecules. *Chem Rev* 121(3):1286–1424
48. Ahmad M, Patel R, Lee DT, Corkery P, Kraetz A, Prerna, Tenney SA, Nykypanchuk D, Tong X, Siepmann JI, Tsapatsis M (2024) ZIF-8 vibrational spectra: peak assignments and defect signals. *ACS Appl Mater Interfaces* 16(21):27887–27897
49. Alharbi FF, Gouadria SM, Alhwali L, Aman S, Farid HMT (2024) Perovskite nanostructure anchored on reduced graphene (rGO) nanosheets as an efficient electrocatalyst for oxygen evolution reaction (OER). *Diam Relat Mater* 148:111456–lh
50. Monama GR, Mdluli SB, Mashao G, Makhafola MD, Ramohlolae KE, Molapo KM, Hato MJ, Makgopa K, Iwuoha EI, Modibane KD (2018) Palladium deposition on copper (II) phthalocyanine/metal organic framework composite and electrocatalytic activity of the modified electrode towards the hydrogen evolution reaction. *Renew Energy* 119:62–72
51. Afkhami-Ardekani M, Naimi-Jamal MR, Doaae S, Rostamnia S (2022) Solvent-free mechanochemical preparation of metal-organic framework ZIF-67 impregnated by Pt nanoparticles for water purification. *Catalysts* 13(1):9
52. Liu D, Li X, Wei L, Zhang T, Wang A, Liu C, Prins R (2017) Disproportionation of hypophosphite and phosphite. *Dalton Trans* 46(19):6366–6378
53. Makhafola MD, Modibane KD, Ramohlolae KE, Maponya TC, Hato MJ, Makgopa K, Iwuoha EI (2021) Palladinized graphene oxide-MOF induced coupling of Volmer and Heyrovsky mechanisms, for the amplification of the electrocatalytic efficiency of hydrogen evolution reaction. *Sci Rep* 11(1):17219
54. Makhafola MD, Ramohlolae KE, Maponya TC, Somo TR, Iwuoha EI, Makgopa K, Hato MJ, Molapo KM, Modibane KD (2020) Electrocatalytic activity of graphene oxide/metal organic framework hybrid composite on hydrogen evolution reaction properties. *Int J Electrochem Sci* 15(6):4884–4899
55. Leifeld J, Franko U, Schulz E (2006) Thermal stability of soil organic matter responds to long-term fertilization practices. *Biogeosciences Discuss* 3(2):309–320
56. Priestley IJG, Brown P, Ledru J, Charsley E (2008) Thermal stability at elevated pressure—an investigation using differential scanning calorimetry. In *INSTITUTION OF CHEMICAL*

- ENGINEERS SYMPOSIUM SERIES (Vol. 154, p. 717). Institution of Chemical Engineers; 1999
57. Kasana S, Nigam V, Singh S, Kurmi BD, Patel P (2024) A new insight into the Huisgen reaction: heterogeneous copper catalyzed azide–alkyne cycloaddition for the synthesis of 1, 4-disubstituted triazole (from 2018–2023). *Chem Biodivers.* <https://doi.org/10.1002/cbdv.202400109>
 58. Chrissafis K, Bikiaris D (2011) Can nanoparticles really enhance thermal stability of polymers? Part I: an overview on thermal decomposition of addition polymers. *Thermochim Acta* 523(1–2):1–24
 59. Rasool N, Alqarni AS, Ahmad K, Al-Sehemi AG, Henaih AMA, Aman S (2024) Enhancement of BaCeO₃ OER performance by generating a nanohybrid with gCN for electrochemical water splitting. *Int J Hydrg Energy* 81:562–572
 60. Alharbi FF, Alahmari SD, Aman S, Dahshan A, Henaih AMA (2024) Developing TiCo₂O₄ spinel based on rGO nanosheet to enhance electrochemical performance of OER activity. *J Electroanal Chem* 963:118299
 61. Kumar A, Sadanandhan AM, Jain SL (2019) Silver doped reduced graphene oxide as a promising plasmonic photocatalyst for oxidative coupling of benzylamines under visible light irradiation. *New J Chem* 43(23):9116–9122
 62. Maheen A, Alsalhi SA, Tahir K, Kumar A, Sharma RSK, Pathak PK, Saini S, Pandey VK, Haldhar R (2025) Enhancement of MnTe electrocatalytic properties via Sm doping strategy employed for OER application. *J Sol-Gel Sci Technol.* <https://doi.org/10.1007/s10971-025-06670-3>
 63. Bibi I, Elaissi S, Aldhafeeri TR, Ali SK, Tahir K, Kumar A (2025) Facile fabrication of CdAl₂O₄ adorned on polyaniline for improving oxygen evolution process in basic media. *Transition Met Chem.* <https://doi.org/10.1007/s11243-025-00651-9>
 64. Liu Y, Li L, Liu L, Wang L, Zang M, Zhou X, Azam M, Tai X (2025) Bimetallic Au–Ru nanoparticles supported on zeolitic imidazolate framework-67 as highly efficient catalysts for the selective oxidation of benzyl alcohol. *Sci Rep* 15(1):12145
 65. Meng H, Chen Z, Zhu J, You B, Ma T, Wei W, Vernuccio S, Xu J, Ni BJ (2024) In situ amorphization of electrocatalysts. *Adv Funct Mater* 34(39):2405270
 66. Bennett TD, Keen DA, Tan JC, Barney ER, Goodwin AL, Cheetham AK (2011) Thermal amorphization of zeolitic imidazolate frameworks. *Angew Chem Int Ed* 50(13):3067–3071
 67. Shahsavari M, Mortazavi M, Tajik S, Sheikholeslami I, Beitollahi H (2022) Synthesis and characterization of GO/ZIF-67 nanocomposite: investigation of catalytic activity for the determination of epinephrine in the presence of Dobutamine. *Micromachines* 13(1):88
 68. Pattengale BA (2018) *The Photodynamic and Structural Analyses of Advanced Materials for Solar Fuel Conversion* (Doctoral dissertation, Marquette University)
 69. Mustapha S, Tijani JO, Ndamito MM, Abdulkareem AS, Shuaib DT, Amigun AT, Abubakar HL (2021) Facile synthesis and characterization of TiO₂ nanoparticles: X-ray peak profile analysis using Williamson–Hall and Debye–Scherrer methods. *Int Nano Lett* 11(3):241–261
 70. Monama GR, Ramoroka ME, Ramohlolwa KE, Seleka MW, Iwuoha EI, Modibane KD (2024) Terbium-and samarium-doped Li₂ZrO₃ perovskite materials as efficient and stable electrocatalysts for alkaline hydrogen evolution reactions. *Environ Sci Pollut Res* 31(42):54920–54937
 71. Cao Q, Gao Y, Pu J, Elshahawy AM, Guan C (2024) Materials and structural design for preferable Zn deposition behavior toward stable Zn anodes. *SmartMat* 5(1):e1194
 72. Pinjari S, Bera T, Kjeang E (2023) Room temperature hydrogen storage enhancement in copper-doped zeolitic imidazolate frameworks with trioctylamine. *Sustain Energy Fuels* 7(13):3142–3151
 73. Chen Q, Jia Y, Xie S, Xie Z (2016) Well-faceted noble-metal nanocrystals with nonconvex polyhedral shapes. *Chem Soc Rev* 45(11):3207–3220
 74. Coppens MO (1999) The effect of fractal surface roughness on diffusion and reaction in porous catalysts—from fundamentals to practical applications. *Catal Today* 53(2):225–243
 75. Nandiyanto ABD, Okuyama K (2011) Progress in developing spray-drying methods for the production of controlled morphology particles: from the nanometer to submicrometer size ranges. *Adv Powder Technol* 22(1):1–19
 76. Winter M, Brodd RJ (2004) What are batteries, fuel cells, and supercapacitors? *Chem Rev* 104(10):4245–4270
 77. Afzali E, Mirjafary Z, Akbarzadeh A, Saeidian H (2023) Functionalized layered double hydroxide–zeolitic imidazolate nanoreactor with active sites of multi-source copper (II) as an efficient nanocatalyst for Huisgen and Pechmann reactions. *J Inorg Organomet Polym Mater* 33(10):3282–3292
 78. Belenov S, Pavletts A, Paperzh K, Mauer D, Menshikov V, Alekseenko A, Pankov I, Tolstunov M, Guterman V (2023) The PtM/C (M=Co, Ni, Cu, Ru) electrocatalysts: their synthesis, structure, activity in the oxygen reduction and methanol oxidation reactions, and durability. *Catalysts* 13(2):243
 79. Zhu J, Tai J, Liu T, Wang Y, Li Y, Yang M, Ma D, Deng L, Luo J, Zhang P (2025) Emerging Zinc-ion capacitor science: compatible principle, design paradigm, and frontier applications. *Adv Energy Mater.* <https://doi.org/10.1002/aenm.202403739>
 80. Ahmad A, Iqbal N, Noor T, Hassan A, Khan UA, Wahab A, Raza MA, Ashraf S (2021) Cu-doped zeolite imidazole framework (ZIF-8) for effective electrocatalytic CO₂ reduction. *J CO₂ Util* 48:101523
 81. Ren X, Lv Q, Liu L, Liu B, Wang Y, Liu A, Wu G (2020) Current progress of Pt and Pt-based electrocatalysts used for fuel cells. *Sustain Energy Fuels* 4(1):15–30
 82. Zhang X, Li H, Yang J, Lei Y, Wang C, Wang J, Tang Y, Mao Z (2021) Recent advances in Pt-based electrocatalysts for PEMFCs. *RSC Adv* 11(22):13316–13328
 83. Chen J, Ha Y, Wang R, Liu Y, Xu H, Shang B, Wu R, Pan H (2022) Inner Co synergizing outer Ru supported on carbon nanotubes for efficient pH-universal hydrogen evolution catalysis. *Nano-Micro Lett* 14(1):186
 84. Li L, Tian F, Qiu L, Wu F, Yang W, Yu Y (2023) Recent progress on ruthenium-based electrocatalysts towards the hydrogen evolution reaction. *Catalysts* 13(12):1497
 85. Osman AI, Abd-Elaziz W, Nasr M, Farghali M, Rashwan AK, Hamada A, Wang YM, Darwish MA, Sebaey TA, Khatab A, Elsheikh AH (2024) Enhanced hydrogen storage efficiency with sorbents and machine learning: a review. *Environ Chem Lett.* <https://doi.org/10.1007/s10311-024-01741-3>
 86. Wu F, Wang C, Liao K, Shao Z (2023) Air cathode design for light-assisted charging of metal–air batteries: recent advances and perspectives. *Energy Fuels* 37(13):8902–8918
 87. Montella C, Tezyk V, Effori E, Laurencin J, Siebert E (2021) Linear sweep and cyclic voltammetry of porous mixed conducting oxygen electrode: formal study of insertion, diffusion and chemical reaction model. *Solid State Ionics* 359:115485
 88. Mikolajczyk T, Pierozynski B, Smoczynski L, Wiczkowski W (2018) Electrodegradation of resorcinol on pure and catalyst-modified Ni foam anodes, studied under alkaline and neutral pH conditions. *Molecules* 23(6):1293
 89. González-Meza OA, Larios-Durán ER, Gutiérrez-Becerra A, Casillas N, Escalante JI, Bárcena-Soto M (2019) Development of a Randles–Ševčík-like equation to predict the peak current of cyclic voltammetry for solid metal hexacyanoferrates. *J Solid State Electrochem* 23:3123–3133
 90. Henstridge MC, Laborda E, Dickinson EJ, Compton RG (2012) Redox systems obeying Marcus–Hush–Chidsey electrode

- kinetics do not obey the Randles–Ševčík equation for linear sweep voltammetry. *J Electroanal Chem* 664:73–79
91. Qian X, Wu Y, Kan M, Fang M, Yue D, Zeng J, Zhao Y (2018) FeOOH quantum dots coupled g-C₃N₄ for visible light driving photo-Fenton degradation of organic pollutants. *Appl Catal B* 237:513–520
92. Safizadeh F, Ghali E, Houlachi G (2015) Electrocatalysis developments for hydrogen evolution reaction in alkaline solutions—a review. *Int J Hydrog Energy* 40(1):256–274
93. Seleka WM, Ramohlola KE, Modibane KD, Makhado E (2024) Quaternary conducting Cs/GO/PANi hydrogel composites: a smart material for room temperature hydrogen sensing. *Diamond Relat Mater* 146:111156
94. Wei C, Sun S, Mandler D, Wang X, Qiao SZ, Xu ZJ (2019) Approaches for measuring the surface areas of metal oxide electrocatalysts for determining their intrinsic electrocatalytic activity. *Chem Soc Rev* 48(9):2518–2534
95. Shrestha NK, Patil SA, Han J, Cho S, Inamdar AI, Kim H, Im H (2022) Chemical etching induced microporous nickel backbones decorated with metallic Fe@ hydroxide nanocatalysts: an efficient and sustainable OER anode toward industrial alkaline water-splitting. *J Mater Chem A* 10(16):8989–9000
96. Zhu Y, Klingenhof M, Gao C, Koketsu T, Weiser G, Pi Y, Liu S, Sui L, Hou J, Li J, Jiang H (2024) Facilitating alkaline hydrogen evolution reaction on the hetero-interfaced Ru/RuO₂ through Pt single atoms doping. *Nat Commun* 15(1):1447
97. Plevova M, Hnat J, Bouzek K (2021) Electrocatalysts for the oxygen evolution reaction in alkaline and neutral media. A comparative review. *J Power Sources* 507:230072
98. Zlatar M, Escalera-Lopez D, Rodriguez MG, Hrbek T, Götz C, Joy M, Savan R, Tran A, Nong HP, Pobedinskas HN, P. and, Briega-Martos V (2023) Standardizing OER electrocatalyst benchmarking in aqueous electrolytes: comprehensive guidelines for accelerated stress tests and backing electrodes. *ACS Catal* 13(23):15375–15392
99. Swathi S, Yuvakkumar R, Ravi G, Shanthini M, Al-Sehemi AG, Thambidurai M, Nguyen HD, Velauthapillai D (2022) Effect of sodium dodecyl sulfate surfactant concentrations on the novel strontium copper oxide nanostructures for enriching hydrogen evolution reaction electrochemical activity in alkaline solution. *J Alloy Compd* 928:167001
100. Hussain S, Akbar K, Vikraman D, Rabani I, Song W, An KS, Kim HS, Chun SH, Jung J (2021) Experimental and theoretical insights to demonstrate the hydrogen evolution activity of layered platinum dichalcogenides electrocatalysts. *J Mater Res Technol* 12:385–398
101. Li Y, Wang H, Xie L, Liang Y, Hong G, Dai H (2011) *MoS₂* nanoparticles grown on graphene: an advanced catalyst for the hydrogen evolution reaction. *J Am Chem Soc* 133(19):7296–7299
102. Guo F, Macdonald TJ, Sobrido AJ, Liu L, Feng J, He G (2023) Recent advances in ultralow-Pt-loading electrocatalysts for the efficient hydrogen evolution. *Adv Sci* 10(21):2301098
103. Qi H (2025) Alloyed single-atom catalysts for electro- and photocatalytic water splitting. *Chemical Synthesis*, 5
104. Li X, Li J, Kurbanjan D, Yu T, Du H (2023) Nickel-doped Co₃O₄ electrocatalyst derived from bimetal zeolitic imidazolate frameworks for the oxygen evolution reaction of electrolysis. *Appl Organomet Chem* 37(4):e7006
105. Kale HB, Kute AD, Gaikwad RP, Fornasiero P, Zbořil R, Gawande MB (2024) Synthesis and energy applications of copper-based single-atom electrocatalysts. *Coord Chem Rev* 502:215602
106. Wang Y, Wang Y, Zhang L, Liu CS, Pang H (2019) Core-shell-type ZIF-8@ ZIF-67@ POM hybrids as efficient electrocatalysts for the oxygen evolution reaction. *Inorg Chem Front* 6(9):2514–2520
107. Gao H, Han F, Yi S, Chen L, Chen D (2023) OER catalyst fabricated with ZIF-67 derived carbon and selectively exsolvated perovskite oxide. *J Alloy Compd* 963:170908
108. Qi R, Liu X, Bu H, Niu X, Ji X, Ma J, Gao H (2023) In situ growth of phosphorized ZIF-67-derived amorphous CoP/Cu₂O@ CF electrocatalyst for efficient hydrogen evolution reaction. *Front Chem Sci Eng* 17(10):1430–1439
109. Khaligh A, Sheidaei Y, Tuncel D (2021) Covalent organic framework constructed by clicking azido porphyrin with perpropargyloxy-cucurbit [6] uril for electrocatalytic hydrogen generation from water splitting. *ACS Appl Energy Mater* 4(4):3535–3543
110. Rossi R, Pant D, Logan BE (2020) Chronoamperometry and linear sweep voltammetry reveals the adverse impact of high carbonate buffer concentrations on anode performance in microbial fuel cells. *J Power Sources* 476:228715
111. Marques CL (2021) *Theoretical Analysis of a Potentiostat for Studying Microbial Fuel Cells* (Master's thesis, Universidade da Beira Interior (Portugal))
112. Yang I, Kim SG, Kwon SH, Kim MS, Jung JC (2017) Relationships between pore size and charge transfer resistance of carbon aerogels for organic electric double-layer capacitor electrodes. *Electrochim Acta* 223:21–30
113. Peng S, Li L, Tan H, Cai R, Shi W, Li C, Mhaisalkar SG, Srinivasan M, Ramakrishna S, Yan Q (2014) MS2 (M=Co and Ni) hollow spheres with tunable interiors for high-performance supercapacitors and photovoltaics. *Adv Funct Mater* 24(15):2155–2162
114. Bredar AR, Chown AL, Burton AR, Farnum BH (2020) Electrochemical impedance spectroscopy of metal oxide electrodes for energy applications. *ACS Appl Energy Mater* 3(1):66–98
115. Ramaripa PS, Modibane KD, Makgopa K, Seerane OA, Mabane-Nkadimeng MS, Makhado E, Pandey S (2023) Influence of phthalocyanine nanowire dye on the performance of titanium dioxide-metal organic framework nanocomposite for dye-sensitized solar cells. *Chem Eng J Adv* 14:100485
116. Ramohlola KE, Masikini M, Mdluli SB, Monama GR, Hato MJ, Molapo KM, Iwuoha EI, Modibane KD (2017) Electrocatalytic hydrogen production properties of polyaniline doped with metal-organic frameworks. *Carbon-related Mater Recognit Nobel Lectures Prof Akira Suzuki ICCE*, pp.373–389
117. Nekouei RK, Mofarah SS, Maroufi S, Tudela I, Sahajwalla V (2022) Determination of the optimum potential window for super- and pseudocapacitance electrodes via in-depth electrochemical impedance spectroscopy analysis. *J Energy Storage* 56:106137
118. Peng Y, Xu J, Xu J, Ma J, Bai Y, Cao S, Zhang S, Pang H (2022) Metal-organic framework (MOF) composites as promising materials for energy storage applications. *Adv Colloid Interface Sci* 307:102732
119. Chen Q, Ranaweera R, Luo L (2018) Hydrogen bubble formation at hydrogen-insertion electrodes. *J Phys Chem C* 122(27):15421–15426
120. Fernandez D, Maurer P, Martine M, Coey JMD, Möbius ME (2014) Bubble formation at a gas-evolving microelectrode. *Langmuir* 30(43):13065–13074
121. Yang X, Karnbach F, Uhlemann M, Odenbach S, Eckert K (2015) Dynamics of single hydrogen bubbles at a platinum microelectrode. *Langmuir* 31(29):8184–8193
122. Monzon LM, Gillen AJ, Mobius ME, Coey JMD (2015) Effect of tetraalkylammonium cations on gas coalescence at a hydrogen-evolving microelectrode. *Langmuir* 31(21):5738–5747
123. Banham D, Zou J, Mukerjee S, Liu Z, Yang D, Zhang Y, Peng Y, Dong A (2021) Ultralow platinum loading proton exchange membrane fuel cells: performance losses and solutions. *J Power Sources* 490:229515
124. Guoa Y (2007) Supplementary Material (ESI) for Journal of Materials Chemistry A

125. Xia L, Ni M, Xu Q, Xu H, Zheng K (2021) Optimization of catalyst layer thickness for achieving high performance and low cost of high temperature proton exchange membrane fuel cell. *Appl Energy* 294:117012
126. Sundriyal S, Shrivastav V, Kaur H, Mishra S, Deep A (2018) High-performance symmetrical supercapacitor with a combination of a ZIF-67/rGO composite electrode and a redox additive electrolyte. *ACS Omega* 3(12):17348–17358
127. Rabani I, Lee JW, Lim T, Truong HB, Nisar S, Afzal S, Seo YS (2024) Construction of a uniform zeolitic imidazole framework (ZIF-8) nanocrystal through a wet chemical route towards supercapacitor application. *RSC Adv* 14(1):118–130
128. Jeong HS, Sahoo G, Jeong SM (2023) Surface-engineered carbon nanofibers enriched with metallic particles for effective bimetallic MOF formation toward hybrid supercapacitors. *J Energy Storage* 73:109260
129. Zhou H, Cao W, Sun N, Jiang L, Liu Y, Pang H (2021) Formation mechanism and properties of NiCoFeLDH@ ZIF-67 composites. *Chin Chem Lett* 32(10):3123–3127

Publisher's Note Springer Nature remains neutral with regard to jurisdictional claims in published maps and institutional affiliations.

Springer Nature or its licensor (e.g. a society or other partner) holds exclusive rights to this article under a publishing agreement with the author(s) or other rightsholder(s); author self-archiving of the accepted manuscript version of this article is solely governed by the terms of such publishing agreement and applicable law.